Equilibrium reconstruction in an iron core tokamak using a deterministic magnetisation model

# Equilibrium reconstruction in an iron core tokamak using a deterministic magnetisation model

L C Appel[1], I Lupelli[1,2] and JET Contributors[3]

[1]*CCFE, Culham Science Centre, Abingdon, Oxfordshire, OX14 3DB, UK*

[2]*Univeristy of Rome "Tor Vergata", Dep. of Industrial Engeneering, Via del Politecnico 1, 00133, Rome, Italy*

[3]*EUROfusion Consortium, JET, Culham Science Centre, Abingdon, Oxfordshire, OX14 3DB, UK*

**Abstract**

In many tokamaks ferromagnetic material, usually referred to as an iron-core, is present in order to improve the magnetic coupling between the solenoid and the plasma. The presence of the iron core in proximity to the plasma changes the magnetic topology with consequent effects on the magnetic field structure and the plasma boundary. This paper considers the problem of obtaining the free-boundary plasma equilibrium solution in the presence of ferromagnetic material based on measured constraints. The current approach employs a model described by O'Brien et al.[1] in which the magnetization currents at the air-iron boundary are represented by a set of free parameters and appropriate boundary conditions are enforced via a set of quasi-measurements on the material boundary. This can lead to the possibility of overfitting the data and hiding underlying issues with the measured signals. Although the model typically achieves good fits to measured magnetic signals there are significant discrepancies in the inferred magnetic topology compared with other plasma diagnostic measurements that are independent of the magnetic field. An alternative approach for equilibrium reconstruction in iron-core tokamaks, termed the deterministic magnetisation model is developed and implemented in EFIT++. The iron is represented by a boundary current with the gradients in the magnetisation dipole state generating macroscopic internal magnetisation currents. A model for the boundary magnetisation currents at the iron-air interface is developed using B-Splines enabling continuity to arbitrary order; internal magnetisation currents are allocated to triangulated regions within the iron, and a method to enable adaptive refinement is implemented. The deterministic model has been validated by comparing it with a synthetic 2-D electromagnetic model of JET. It is established that the maximum field discrepancy is less than 1.5mT throughout the vacuum region enclosing the plasma. The discrepancies of simulated magnetic probe signals are accurate to within 1% for signals with absolute magnitude greater than 100mT; in all other

*Email address:* lynton.appel@ukaea.uk (L C Appel[1], I Lupelli[1,2] and JET Contributors[3] )

See the author list of Overview of the JET results in support to ITER by X. Litaudon et al. to be published in Nuclear Fusion Special issue: overview and summary reports from the 26th Fusion Energy Conference (Kyoto, Japan, 17-22 October 2016)

cases agreement is to within 1mT. The effect of neglecting the internal magnetisation currents increases the maximum discrepancy in the vacuum region to >20mT, resulting in errors of 5-10% in the simulated probe signals. The fact that the previous model neglects the internal magnetisation currents (and also has additional free parameters when fitting the measured data) makes it unsuitable for analysing data in the absence of plasma current. The discrepancy of the poloidal magnetic flux within the vacuum vessel is to within 0.1Wb. Finally the deterministic model is applied to an equilibrium force-balance solution of a JET discharge using experimental data. It is shown that the discrepancies of the outboard separatrix position, and the outer strike-point position inferred from Thomson Scattering and Infrared camera data are much improved beyond the routine equilibrium reconstruction, whereas the discrepancy of the inner strike-point position is similar.

---

**Keywords**

tokamak; magnetic; equilibrium reconstruction; ferromagnetic

## 1. Introduction

Accurate knowledge of the magnetic field structure in a tokamak is a prerequisite first step for the analysis and control of plasma discharges. In order to improve the magnetic coupling between the solenoid and the plasma many tokamaks (eg. JET[1], ISTTOK[2], Tore Supra[3], STOR-M[4], TEXT[5]) incorporate a ferromagnetic core, usually referred to as an iron core. The presence of the iron core in proximity to the plasma changes the magnetic topology with consequent effects on the plasma boundary shape. From the numerical point of view the presence of the iron core represents a complication by adding an additional non-linearity to the calculation of equilibrium force-balance. This calculation in tokamaks, based on measured constraints, known as *equilibrium reconstruction* is carried out by codes such as EFIT[6, 7], EQUAL[8, 9], CLISTE[10] and EQUINOX[11, 12, 13].

This paper considers the case of the JET tokamak using EFIT++[14]. The code is used for equilibrium reconstruction on JET between discharges (ie. during *intershot* operation) and in subsequent detailed interpretive analyses. The EFIT++ code, based on the algorithm of EFIT[6], is machine-agnostic, written mainly in C++ and was developed at JET and the Culham Centre for Fusion Energy. Originally the EFIT++ code implemented a magnetisation model based on [1]. For the computation of equilibrium reconstructions carried out between discharges the boundary magnetisation currents (at the air-iron interface) are represented by a set of free parameters and appropriate boundary conditions are enforced via a set of quasi-measurements on the material boundary. These quasi-measurements are used in a $\chi^2$ minimization together with other measurements (typically magnetic flux, local magnetic field and power supply currents) to determine the equilibrium reconstruction based only on magnetic data. This is the so-called EFIT++ fitting model. The advantage of running EFIT++ in this manner is that it is fast, typically 0.1-1s per time-slice. The rapid execution time is a result of the boundary iron magnetisation being represented by comparatively few

discrete piecewise constant currents. This is possible because the iron currents are adjusted during the $\chi^2$ minimization, the purpose being to get a strong fit to the diagnostics in the proximity of the plasma. Furthermore, only the iron boundary closest to the plasma is included. Including the boundary currents as additional degrees of freedom in the $\chi^2$ fit can significantly increase the number of free parameters, particularly because the number of boundary curents is generally much greater than the number of free parameters from the other current sources. This can lead to the possibility of overfitting the data and hiding underlying issues with the measured signals: although the EFIT++ fitting model typically achieves good fits to measured magnetic signals there are significant discrepancies in the inferred magnetic topology compared with other plasma diagnostic measurements. In this work we present an alternative approach for equilibrium reconstruction in iron core tokamaks, termed the deterministic model. The iron is represented by a boundary current with the gradients in the magnetisation dipole state generating macroscopic internal magnetisation currents. A model for the boundary magnetisation currents at the iron-air interface is developed using B-Splines enabling continuity to arbitrary order; internal magnetisation currents are allocated to triangulated regions within the iron, and a method to enable adaptive refinement is implemented. This model is strongly based on the underlying physics described by Maxwell's equations coupled with the constitutive relations of the ferromagnetic materials. Therefore, the magnetisation currents, both the boundary and internal currents, are enforced exactly and do not appear as quasi-measurements in the $\chi^2$ minimisation. Compared to the fitting model there are no quasi-measurements enabling improved interpretation of the real measurements. A practical implication of this is to enable the possibility of carrying out in-vessel calibration of the magnetic diagnostic system to improve the consistency of the model against the experimental data in iron-core toakamaks. Section 2 summarises the key components of the EFIT++ algorithm followed by a derivation of the current distribution in a ferromagnetic material. Section 3 develops a model for the representation of boundary magnetisation currents at the air-iron interface. Section 4 describes the implementation of the internal magnetisation currents. Section 5 validates the deterministic model by comparing it with a synthetic 2-D electromagnetic model of JET. Finally section 6 describes the use of the EFIT++ deterministic model on an equilibrium force-balance solution of a JET discharge using only magnetic signals; results are compared with other independent diagnostic measurements.

## 2. EFIT++ equilibrium force-balance algorithm in presence of ferromagnetic material

The EFIT++ algorithm sets out to provide an equilibrium force balance solution that is consistent with measurements whilst taking into account the presence of ferromagnetic material. The flow diagram of the EFIT++ algorithm, valid for both the fitting and the deterministic iron models, is illustrated in figure 1a. The programme enters a loop which iterates towards a converged equilibrium force balance solution by successively invoking the magnetisation model, the linearised Grad-Shafranov solver and a least-squares algorithm to update values of poloidal field circuit currents and coefficients of the plasma-based flux functions defined below. Optionally there may

be an inner loop to improve the convergence of the magnetisation model. Below we summarise the algorithm.

The state of axisymmetric equilibrium force balance in a tokamak is encapsulated in the Grad-Shafranov equation:

$$\Delta^* \psi_p \quad = \quad -2\mu_0 R J_\phi \tag{1}$$

The equation, expressed in right-handed cylindrical coordinates ($R$,$\phi$,$Z$), is written in terms of poloidal flux $\psi_p$=$RA_\phi$ where $A_\phi$ is the toroidal component of the magnetic vector potential[15], and toroidal current density, $J_\phi$, which can itself be expressed as a function of two plasma-based flux functions, $p(\psi_p)$ and $f(\psi_p)$ and a non-plasma based component $J_{\rm ext}$:

$$J_\phi \quad = \quad R\frac{\partial p}{\partial \psi_p} + \frac{1}{\mu_0 R} f \frac{\partial f}{\partial \psi_p} + J_{ext}(R,Z) \tag{2}$$

The parameter $J_{\rm ext} = J_{\rm pf} + J_{\rm induced} + J_{\rm iron}$ in which $J_{\rm pf}$ is associated with the set of $n_{pfc}$ poloidal field circuit currents $\{I_i^{pfc}\}$; $J_{\rm induced}$ is associated with $n_{ind}$ independent induced currents $\{I_i^{ind}\}$; and $J_{\rm iron}$ is associated with $n_{iron}$ independent currents $\{I_i^{iron}\}$. The first two terms on the right hand side of (2) represent the plasma current flowing in a closed region bounded by a magnetic separatrix. The flux functions have the following generic form:

$$p'(\psi_p) \quad = \quad \sum_{i=1}^{n_\alpha} \alpha_i c_i(\bar{\psi}_p) \tag{3}$$

$$ff'(\psi_p) \quad = \quad \sum_{i=1}^{n_\beta} \beta_i d_i(\bar{\psi}_p) \tag{4}$$

where $\{c_i(\bar{\psi}_p)\}$ and $\{d_i(\bar{\psi}_p)\}$ are sets of basis functions; a typical choice is to use $c_i = d_i = \bar{\psi}_p^{i-1}$ but EFIT++ also permits other choices for example tension splines [16] enable more realistic current distributions in advanced reconstructions. This is out of scope of this paper. Here,

$$\bar{\psi}_p \quad = \quad (\psi_p - \psi_0)/(\psi_b - \psi_0) \tag{5}$$

is the normalized poloidal flux where $\psi_b$ and $\psi_0$ are the poloidal flux values at the plasma separatrix and at the magnetic axis [6].

Referring to the EFIT++ flow diagram shown in figure 1 the *Linearised Grad-Shafranov solver* solves (1) with $J_\phi$ constructed using $\bar{\psi}_p$ generated at a previous step[6]. The field solution in the region containing the plasma current is solved using the fast 2-D cyclic reduction finite difference method of Buneman[17]. Having computed a solution for $\psi_p(R,Z)$, the loci of the separatrix and magnetic axis are identified enabling $\bar{\psi}_p$ to be recomputed using (5).

The *Least-Squares Solver* computes updated values for the *current coefficients* $\mathbf{I} = \{\alpha_i\} \cup \{\beta_i\} \cup \{I_i^{pfc}\} \cup \{I_i^{ind}\} \cup \{I_i^{iron}\}$ by finding a solution which minimises

$$\chi^2 = \sum_i \left( \frac{M_i - C_i}{\sigma_i} \right)^2 \tag{6}$$

In the above equation, $M_i$ denotes a measurement (or user designed) constraint value and $\sigma_i$ denotes its associated uncertainty. The parameter $C_i$ expresses a linearised equation for $M_i$ in terms of the current coefficients:

$$C_i = \sum_{j=1}^{n_{pfc}} G_{ij}^{pfc} I_j^{pfc} + \sum_{j=1}^{n_{iron}} G_{ij}^{iron} I_j^{iron} + \sum_{j=1}^{n_{ind}} G_{ij}^{ind} I_j^{ind} + \sum_{j=1}^{n_{\alpha}} G_{ij}^{\alpha} \alpha_j + \sum_{i=1}^{n_{\beta}} G_{ij}^{\beta} \beta_i \quad (7)$$

where the $G_{ij}^{x}$ functions are commonly referred to as response functions. Equation 6 can be expressed in the form (for polynomial basis functions)

$$\chi^2 = \|\mathbf{AI} - \mathbf{b}\| \quad (8)$$

where the $i^{th}$ row of $\mathbf{AI}$ and $\mathbf{b}$ contain respectively $C_i/\sigma_i$ and $M_i/\sigma_i$. Utilising tension splines, equation 8 is supplemented by the exact constraints:

$$\mathbf{CI} - \mathbf{D} = 0 \quad (9)$$

where $\mathbf{C}$ is a rectangular matrix and $\mathbf{D}$ a vector constructed to enforce appropriate interface conditions between spline intervals [18]. In general $\mathbf{A}$ will not be square and the minimum norm of equation 8 is computed using singular value decomposition unless tension splines are employed in which case a constrained least squares solver is used[19].

Figures 1b and 1c plot poloidal flux surfaces for discharges in MAST and JET tokamaks.

### *2.1. Dipole current distribution in a ferromagnetic material*

The macroscopic result of microscopic dipole currents gives rise to the magnetisation vector $\mathbf{M}$[20] and results in a magnetisation current

$$\mathbf{J_m} = \nabla \times \mathbf{M} \quad (10)$$

In terms of the magnetising force $\mathbf{H}$ and relative magnetic permeability $\mu_r$,

$$\mathbf{M} = (\mu_r - 1)\mathbf{H} \quad (11)$$

Substituting,

$$\mathbf{J_m} = \nabla \times [(\mu_r - 1)\mathbf{H}] \quad (12)$$

It is instructive to split this into three separate components. First we consider the interface between the ferromagnetic material and another material where $\mu_r$ is discontinuous. Integrating over an element $\delta\mathbf{x}$ of the boundary yields the *boundary magnetisation* current $I_b$,

$$I_b = \mathbf{J_b} \cdot \delta\mathbf{x} = \oint \mathbf{M} \cdot d\boldsymbol{\ell} \quad (13)$$

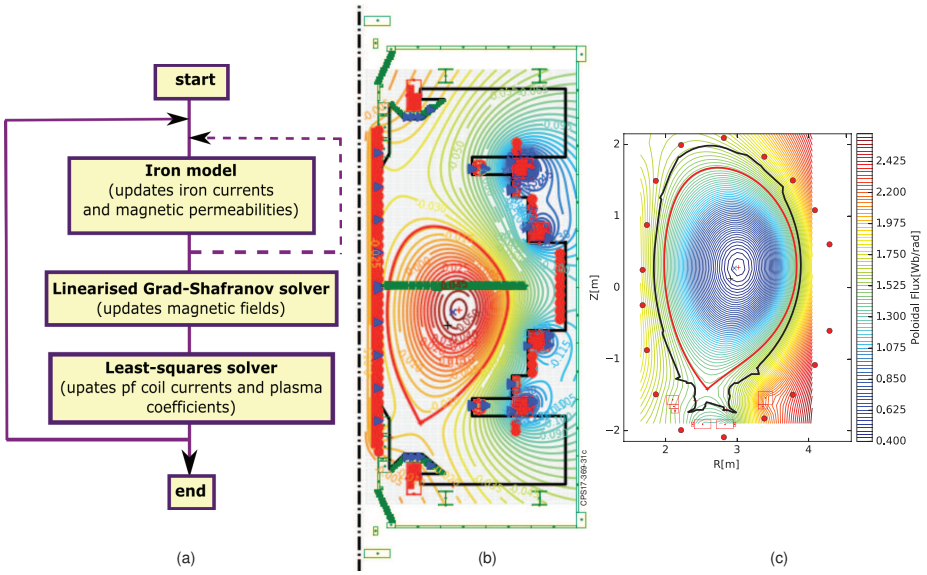


Figure 1: (a) Flow diagram of EFIT++ algorithm; (b) EFIT++ equilibrium reconstruction of discharge 29916 at 240ms on MAST; (c) EFIT++ equilibrium reconstruction of discharge 82783 at 52.9s on JET

in which the integral is evaluated on a path enclosing $\delta\mathbf{x}$. The magnetisation model based on O'Brien[1] only takes account of $\mathbf{J_b}$. This is strictly correct only in the case when $\mu_r$ is constant. In the bulk of the ferromagnetic material,

$$\mathbf{J_m} = \mathbf{J_f} + \mathbf{J}_\mu \tag{14}$$

where

$$\mathbf{J_f} = (\mu_r - 1)\nabla \times \mathbf{H} \tag{15}$$

resembles an enhanced current of free charges in the iron due to the presence of the dipoles. The term is non-zero only when a macroscopic current $\mathbf{J_{iron}} = \nabla \times \mathbf{H}$ flows in the iron and describes a supplementary current $(\mu_r - 1)\mathbf{J_{iron}}$ due to the dipoles. The final term is

$$\mathbf{J}_\mu = \nabla\mu_r \times \mathbf{H}, \tag{16}$$

the dipole current contribution resulting from the spatial variation in magnetic saturation state. For brevity this will be referred to below as the *internal magnetisation current density*. The magnetisation model described in the current work includes the $\mathbf{J}_\mu$ and $\mathbf{J_b}$ components but excludes $\mathbf{J_f}$. The assumption $\mathbf{J_f} = 0$ is reasonable for tokamaks that have a laminated iron-core as is the case for JET.

The EFIT++ model is implemented in cylindrical ($R$, $\phi$, $Z$) geometry assuming axisymmetry as the linearised Grad-Shafranov solver described earlier. Denoting the unit vector ($\hat{\mathbf{R}}$, $\hat{\phi}$, $\hat{\mathbf{Z}}$), $\mathbf{J_m} \times \hat{\phi} = 0$ ie. the only finite components are $J^b_\phi \equiv \mathbf{J_b} \cdot \hat{\phi}$ and $J^\mu_\phi \equiv \mathbf{J}_\mu \cdot \hat{\phi}$ .

## 3. Representation of boundary magnetisation currents at the air-iron interface

The design of the boundary magnetisation current model for $J_\phi^b$ should take into account rapid field and current variations that can occur in the proximity of corners due to the requirement of ensuring that the tangential magnetitzation force **H** is conserved across the material interface (this requirement is stated formally in equation 28). On studies with 2-D elliptic problems, Fix et al. [21] have shown that high order elements are more satisfactory than simply relying on local mesh refinement to model singular functions. The implication is that a 1-D boundary magnetisation current model that uses higher order elements will be more computationally efficient than using lower order elements. The boundary magnetisation model developed in this paper is based on B-splines[22, 23], permitting users to specify continuity at each knot location to any desired order. To further mitigate the effect of singularities users are provided with the ability to model the boundary shape by both straight line segments and arcs.

The deterministic model sets out to enforce magnetic boundary conditions either over the entire extent or over a portion of the material boundary. We will refer to these respectively as *closed* boundaries and *open* boundaries. The latter case is useful for modelling semi-infinite regions and can also be used to reduce the size of the numerical problem if it is unnecessary to implement magnetic continuity conditions over the entire boundary. In cylindrical geometry, the open boundary is used to model boundaries at $R$=0. The description of the magnetisation model below refers to a single boundary, but the implementation in EFIT++ is for multiple boundaries and the extension to that case is straightforward. Figure 9 shows the material boundaries implemented for the JET iron-core. There are three boundaries: an open boundary to represent the central iron pillar and two closed boundaries.

The following section describes the representation of the boundary magnetisation current by B-splines. As is generally the case for all spline representations, the magnetisation is represented as a finite sum of products involving a set of basis functions (equation 22). The basis functions are defined via a set of *knots* and are computed using a recursive relation (equation 23). Whilst the order of the of the B-splines specifies the limiting continuity at knot locations, the continuity at these knots can be reduced by defining multiple knots at the same location. The locations of the knots are referred to as breakpoints; for example figure 10 plots the locations of the breakpoints representing the JET iron boundaries analysed in sections 5 and 6. Section 3.2 describes the EFIT++ model for the boundary magnetisation current.

### *3.1. B-spline representation of the boundary magnetisation current*

We denote the region over which the boundary is defined as $L$, the length of the boundary, $\ell_a$ and the distance around the boundary from a reference position, $\ell$ (see figure 9). In the case of a closed boundary, $\ell = 0$ and $\ell = \ell_a$ represent the same point. The numerical solution for the magnetisation model will be in terms of a variation of $J_\phi^b(\ell)$. In previous work [1] a discrete current representation was used, splitting $L$ into $n$ sub-intervals $L_j = [\ell_j, \ell_{j+1}]$ such that

$$J_\phi^b(\ell) = \sum_{j=1}^{n} \frac{I_j \boldsymbol{\delta}(\ell - \bar{\ell}_j)}{L_j} \tag{17}$$

where $\boldsymbol{\delta}$ denotes the Dirac delta function, $I_j$ is a filamentary current at $\bar{\ell}_j = (\ell_j + \ell_{j+1})/2$ and $L_j = \ell_{j+1} - \ell_j$.

In the present work we use a B-spline representation adopting the syntactic style introduced by[24] which uses the definitions:

- Polynomials of order $k$ (maximum degree $k-1$) are

$$p(x) = a_0 + a_1 x + \ldots + a_{k-1} x^{k-1} \tag{18}$$

- A function which is continuous (on a given interval) together with its derivatives up to order $n$, that is $f(x), Df, \ldots, D^n f$ is said to be of class $C^n$. Then $C^0$ means that only $f$ is continuous and $C^{-1}$ that $f$ is discontinuous.

- Consider the interval $L$ divided into $q$ sub-intervals $L_j = [\xi_j, \xi_{j+1}]$ by a sequence of $q+1$ points $\{\xi_j\}$ in strict ascending order:

$$0 = \xi_1 < \xi_2 < \ldots < \xi_{q+1} \tag{19}$$

  In the case that $L$ lies on a closed boundary, $\xi_1$ and $\xi_{q+1}$ are at the same physical location. The $\xi_j$ will be called *breakpoints* (bps).

- We specify a second sequence of non-negative integers $\nu_j$, $j = 1, \ldots, q+1$ which define the continuity condition $C^{\nu_j - 1}$ at the associated bps $\xi_j$.

- Finally, let us call *knots* another sequence of $m$ points $\{t_i\}$ in ascending order, not necessarily distinct,

$$t_1 \leq t_2 \leq \ldots \leq t_m \tag{20}$$

  associated with $\xi_j$ and $\nu_j$ as follows:

$$\begin{aligned}
t_1 = \ldots = t_{\mu_1} = \xi_1; \quad & \begin{cases} \textit{open boundary:} & \mu_1 = k \\ \textit{closed boundary:} & 1 \leq \mu_1 \leq k \end{cases} \\
& t_{\mu_1+1} = \ldots = t_{\mu_1+\mu_2} = \xi_2; \\
& \ldots \\
t_{p+1} = \ldots = t_{p+\mu_i} = \xi_i; \qquad & p = \sum_{j=1}^{i-1} \mu_j \\
& \ldots \\
t_{n-\mu_{q+1}} = \ldots = t_n = \xi_q; \qquad & n = \sum_{j=1}^{q} \mu_j
\end{aligned} \tag{21}$$

  in which $\mu_j$ is the multiplicity of knots at $\xi_j$ and is given by $\mu_j = k - \nu_j$. An open boundary has $k$ additional knots:

$$t_{n+1} = \ldots = t_{n+k} = \xi_{q+1};$$

The B-spline representation of $J^b_\phi$ is a piece-wise polynomial function expressed in the form

$$J^b_\phi(\ell) = \sum_{j=1}^{n} J_j N^k_j(\ell) \tag{22}$$

where, $N^k_j(\ell)$ is the $j^{th}$ basis function of order $k$ evaluated via the recurrence relation[22, 23]

$$N^k_j(\ell) = \frac{\ell - \ell(t_j)}{\ell(t_{j+k-1}) - \ell(t_j)} N^{k-1}_j(\ell) + \frac{\ell(t_{j+k}) - \ell}{\ell(t_{j+k}) - \ell(t_{j+1})} N^{k-1}_{j+1}(\ell) \tag{23}$$

with the case of $k = 1$ defined

$$N^1_j = \begin{cases} 1 & \ell(t_j) \le \ell < \ell(t_{j+1}) \\ 0 & elsewhere \end{cases} \tag{24}$$

Equation (22), expressed in terms of $n$ independent basis functions and $m = n + \mu_{q+1}$ knots, enforces the continuity condition of up to $C^{k-2}$ at every breakpoint; enforcing higher continuity is generally only possible by representing $J^b_\phi$ with a single polynomial over the entire boundary. To achieve $C^{k-2}$ at the $j^{th}$ breakpoint we assign $\nu_j = k - 1$ and $\mu_j = 1$ . This is the usual practice for interior bps but continuity may need to be reduced for instance if $\xi_j$ is at a cusp. Continuity requirements at the end-points will vary. Here we assume for an open boundary that the requirement is $C^{-1}$ and we put $\nu_1 = \nu_{q+1} = 0$ (ie. $\mu_1 = \mu_{q+1} = k$). In the case of a closed boundary continuity is usually $C^{k-2}$ ie. the same as for interior bps and we put $\nu_1 = k - 1$ (ie. $\mu_1 = 1$). For these cases, $n = q + k - 1$ for an open boundary, and $n = q$ for a closed boundary.

The $N^k_j$ basis function has a positive non-zero value in the range $\ell(t_j) \le \ell < \ell(t_{j+k})$ and is zero elsewhere. Over each interval $\ell(t_j) \le \ell < \ell(t_{j+1})$, exactly $k$ B-splines are non-zero,

$$N^k_i(\ell) \neq 0 \quad \text{for} \quad i = j, \ldots, j + k - 1 \tag{25}$$

Closed regions utilise the transformations $i \to i - n$ for $i > n$. Finally, in each interval $\ell(t_j) \le \ell < \ell(t_{j+1})$,

$$\sum_{i=j}^{j+k-1} N^k_i(\ell) \quad = \quad 1 \tag{26}$$

Figures 2 and 3 show examples of basis functions for the cases $k$=1 and $k$=4. The locations of breakpoints $\{\xi_1, \xi_2, \ldots\}$ and knots $\{t_1, t_2, \ldots\}$ are indicated on the figures. The number of non zero basis functions at any point on the boundary is equal to $k$. The case $k$=1 defines a set of piecewise constant basis functions with $C^{-1}$ continuity at the breakpoints; the basis functions are top hat functions with value 0 or 1. The case $k$=4 achieves $C^2$ continuity at each breakpoint with $\ell > 0$ and $C^{-1}$ continuity at $\ell = 0$.

We note [25] that the error will be bound by

$$\epsilon \sim h^k_j |D^k J^b_\phi(\ell)| \tag{27}$$

where $h_j$ is the width of the interval $L_j$, $\ell \in L_j$ and $D^k$ denotes the $k^{th}$ derivative.

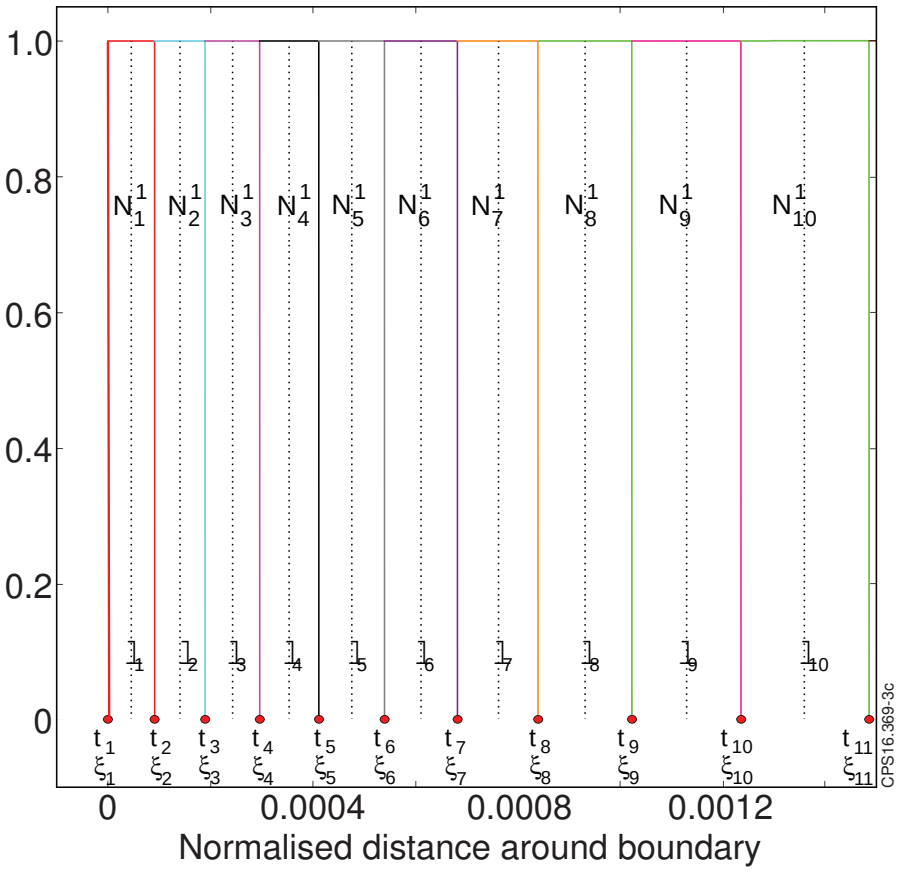


Figure 2: B-spline basis functions with $k = 1$ for the inner boundary shown in figure 9 in the range $0 < \ell/\ell_a < 0.00145$. The locations of the breakpoints $\{\xi_1, \xi_2, \ldots\}$ are indicated by ●; these are also the locations of the knots $\{t_1, t_2, \ldots\}$. The basis function $\{N_1^1, N_2^1, \ldots\}$ are a set of rectangular top-hat functions with peak value 1. The multiplicity of knots at each breakpoint is $\mu = \{1, 1, 1, \ldots\}$; continuity is $C^{-1}$ at each breakpoint. The locations for which the boundary magnetisation model satisfies Ampère's Law (section 3.2) , $\{\ell_1, \ell_2, \ldots\}$ are shown in the figure.

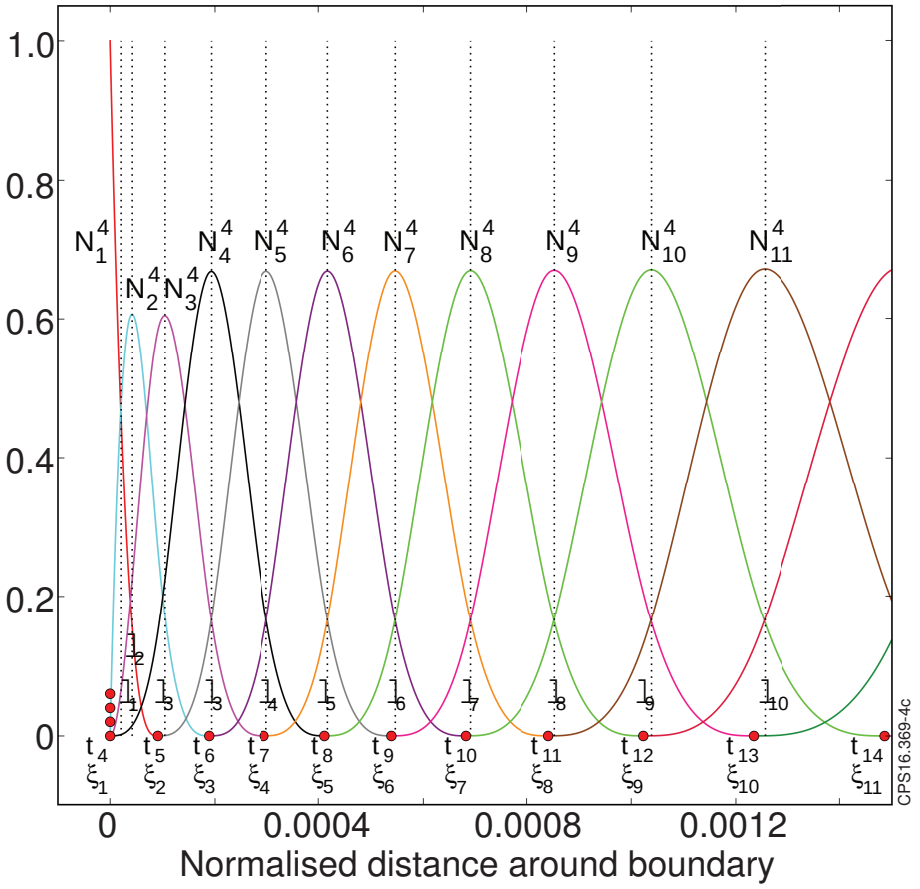


Figure 3: B-spline basis functions with $k = 4$ for the inner boundary shown in figure 9 in the range $0 < \ell/\ell_a < 0.00145$. The locations of the breakpoints $\{\xi_1, \xi_2, \ldots\}$ are indicated by ●; these are also the locations of the knots $\{t_1, t_2, \ldots\}$. The basis function $\{N_1^4, N_2^4, \ldots\}$ are a set of $4^{th}$ order polynomial functions. The multiplicity of knots at each breakpoint is $\mu = \{4, 1, 1, \ldots\}$; continuity is $C^2$ at each breakpoint apart from at $\xi_1$ where continuity is $C^{-1}$. The locations for which the boundary magnetisation model satisfies Ampère's Law (section 3.2) , $\{\ell_1, \ell_2, \ldots\}$ are shown in the figure.

*3.2. Boundary magnetisation current model in EFIT++*

In formulating the magnetisation model, EFIT++ ensures that Ampère's law is satisfied at a set of $r$ distinct *constraint points* $\{\ell_i\}$ within the region $L = [0, \ell_a]$. In the case of a closed boundary, $\ell = 0$ and $\ell = \ell_a$ represent the same point and cannot therefore both be included in $\{\ell_i\}$.

In terms of the magnetising force $\mathbf{H}$, Ampère's law reduces to:

$$\mathbf{H}(\ell_i) \cdot \hat{\boldsymbol{\ell}}_i\Big|_{air} = \mathbf{H}(\ell_i) \cdot \hat{\boldsymbol{\ell}}_i\Big|_{iron} \tag{28}$$

where $\hat{\boldsymbol{\ell}}_i$ is a unit vector tangential to the boundary at $\ell_i$ such that

$$\hat{\boldsymbol{\ell}}_i = \hat{\phi} \times \hat{\mathbf{n}}_i \tag{29}$$

in which $\hat{\mathbf{n}}_i$ is a unit vector normal to the boundary and pointing out of the iron region. In practice this means that coordinates of inner iron-air boundaries are defined anti-clockwise, and outer boundaries are defined clockwise. In the most basic boundary description $\{L_j\}$ are straight line segments. In this case, if $\ell_i$ coincides with the $j^{th}$ breakpoint $\xi_j$, $\hat{\boldsymbol{\ell}}_i$ is taken as the average gradient of the sub-intervals $L_{j-1}$ and $L_j$. This has the effect of rounding corners with the curvature dependent on the location of $\xi_{i-1}$, $\xi_i$ and $\xi_{i+1}$. Finite curvature sub-intervals are also permitted which can eliminate gradient discontinuities. Substituting the constitutive relation $\mathbf{B} = \mu\mathbf{H}$ into (28) yields

$$\mathbf{B}(\ell_i) \cdot \hat{\boldsymbol{\ell}}_i\Big|_{air} = \mathbf{B}(\ell_i) \cdot \hat{\boldsymbol{\ell}}_i/\mu_r(\ell_i)\Big|_{iron} \quad . \tag{30}$$

The magnetic field tangential to the boundary at $\ell_i$ can be written

$$B(\ell_i) = B_{ext}(\ell_i) + \int_0^{\ell_a} J_\phi^b(\ell)\mathbf{G}_\ell(\ell_i;\ell)\, d\ell \tag{31}$$

where $B_{ext}$ is the contribution from the poloidal field coils, the plasma current and induced currents; the integral is the contribution from the magnetisation arising at the material interface with $G_\ell(\ell_i;\ell) = \mathbf{G}(\ell_i;\ell)\cdot\hat{\boldsymbol{\ell}}$ the magnetic field tangential to the boundary at $\ell_i$ due to a unit current at $\ell$. In cylindrical coordinates $\mathbf{G}(\ell_i;\ell)$ can be written

$$\mathbf{G}(\ell_i;\ell)\cdot\hat{\mathbf{R}} = -\frac{2\times10^{-7}\eta\delta Z}{R_i\sqrt{4R_\ell R_i}}\left(-K(\eta) + \frac{R_\ell^2 + R_i^2 + \delta Z^2}{(R_\ell - R_i)^2 + \delta Z^2}E(\eta)\right) \tag{32}$$

$$\mathbf{G}(\ell_i;\ell)\cdot\hat{\mathbf{Z}} = \frac{2\times10^{-7}\eta}{\sqrt{4R_\ell R_i}}\left(K(\eta) + \frac{R_\ell^2 - R_i^2 - \delta Z^2}{(R_\ell - R_i)^2 + \delta Z^2}E(\eta)\right) \tag{33}$$

where $\ell_i \equiv (R_i, Z_i)$, $\ell \equiv (R_\ell, Z_\ell)$, $\delta Z = Z_\ell - Z_i$ and

$$\eta^2 = \frac{4R_\ell R_i}{(R_i + R_\ell)^2 + \delta Z^2} \tag{34}$$

$K(\eta)$ and $E(\eta)$ are complete elliptic integrals of the first and second kind respectively defined

$$K(\eta) = \int_0^{\pi/2} \frac{d\theta}{\sqrt{1 - \eta^2\sin^2\theta}} \tag{35}$$

$$E(\eta) = \int_0^{\pi/2} \sqrt{1 - \eta^2\sin^2\theta}\, d\theta \tag{36}$$

Substituting (22) into (31) and applying (25),

$$B(\ell_i) = \quad B_{ext}(\ell_i) + \sum_{p=1}^{m-1} \int_{\ell(t_p)}^{\ell(t_{p+1})} \sum_{j=p}^{p+k-1} J_j N_j^k(\ell) G_\ell(\ell_i;\ell)\, d\ell \tag{37}$$

The second term is expressed as the contribution of $J_\phi^b(\ell)$ over each of $m-1$ knot intervals; within each interval there are $k$ non-zero basis functions. Alternatively, expressed as a summation from the $n$ basis functions,

$$B(\ell_i) = \quad B_{ext}(\ell_i) + \sum_{j=1}^{n} \int_{\ell(t_j)}^{\ell(t_{j+k})} J_j N_j^k(\ell) G_\ell(\ell_i;\ell)\, d\ell \tag{38}$$

In this case the integral expresses the contribution from the $j^{th}$ basis function over the range of the $k+1$ knots for which it is non-zero. Special care is required to evaluate the integral in the neighbourhood of $\ell = \ell_i$ where $G_\ell(\ell_i;\ell)$ is singular. A zero curvature contribution arises from consideration of the singular point where $\ell = \ell_i$; application of Ampère's law expressed in integral form yields

$$\delta I_0 = \frac{\lambda \mu_0}{2} \sum_{j=p^*}^{p^*+k-1} J_j N_j^k(\ell_i) \tag{39}$$

with $\lambda$=+1 on the air-side of the material and $\lambda$=-1 on the iron-side and in which $\ell(t_{p^*}) \le \ell_i < \ell(t_{p^*+1})$ . The finite curvature contribution is contained in the remainder of the integral excluding the singular point. Combining (38) and (39), the total magnetic field is

$$B(\ell_i) = \quad B_{ext}(\ell_i) + \delta I_0 + \sum_{j=1}^{n} \int_{\Gamma_j} J_j N_j^k(\ell) G_\ell(\ell_i;\ell)\, d\ell \tag{40}$$

where $\Gamma_j = [\ell(t_j), \ell_i)+(\ell_i, \ell(t_{j+k})]$ for $\ell(t_j) \le \ell_i < \ell(t_{j+k})$ and otherwise $\Gamma_j = [\ell(t_j), \ell(t_{j+k})]$. (Here, [] and () indicate closed and open intervals respectively.) Evaluation of the integral in (40) for the case of a semi-open interval employs Romberg integration using the extended midpoint rule[26]. We note in passing that the magnetisation model described in[1] neglects the finite curvature contribution of line-segments enclosing singularities. Although strictly incorrect, this component is small for large $n$.

Substituting (40) into (30) yields a set of $r$ equations

$$\underline{\underline{\mathbf{C}}}\mathbf{J} = \mathbf{E} \tag{41}$$

where $\underline{\underline{\mathbf{C}}}$ is an $r \times n$ matrix:

$$\underline{\underline{\mathbf{C}}} = \begin{pmatrix} C_{1,1} & \cdots & C_{1,n} \\ \vdots & \ddots & \vdots \\ C_{r,1} & \cdots & C_{r,n} \end{pmatrix} \tag{42}$$

in which

$$C_{i,j} \quad = \quad (\mu_r(\ell_i) - 1) \int_{\Gamma_j} N_j^k(\ell) G_\ell(\ell_i;\ell)\, d\ell + \frac{(\mu_r(\ell_i)+1)\,\mu_0}{2} \sum_{j^*=p^*}^{p^*+k-1} \delta(j-j^*) N_j^k(\ell_i) \tag{43}$$

where $\Gamma_j$ and $p^*$ are defined above. $\mathbf{E}$ is a column vector of length $r$ with elements $(e_1, e_2, \ldots, e_r)$ for which

$$e_i = (1 - \mu_r(\ell_i))B_{ext}(\ell_i) \tag{44}$$

and

$$\mathbf{J} = \begin{pmatrix} J_1 \\ \vdots \\ J_n \end{pmatrix} \tag{45}$$

The constraint points $\{\ell_i\}$ should be suitably distributed to ensure that (41) is well conditioned; a useful prescription is to place them at the peak of each basis function; in this case $r = n$ and the matrix $\underline{\underline{\mathbf{C}}}$ is square. Finally, to minimise local variations of the numerical error in $J^b_\phi$, the knot spacing should be chosen according to (27):

$$h(\ell) \propto \left( \frac{1}{|D^k J^b_\phi(\ell)|} \right)^{1/k} \tag{46}$$

indicating that knots should be concentrated in regions of higher gradients, whilst higher order splines will generally enable larger knot spacings to achieve a given accuracy. EFIT++ permits breakpoint spacing according to:

$$\{0, h^\alpha, (2h)^\alpha, \ldots, (n-1)^\alpha h^\alpha\} \tag{47}$$

with the user specifying $h$ and $(n-1)^\alpha h^\alpha - (n-2)^\alpha h^\alpha$.

To illustrate the use of the EFIT++ iron model, we consider a simple case of a single filament carrying 10MA close to a corner material boundary in which the B-H characteristic is shown in figure 4. Figure 5 plots the poloidal flux surfaces. Two cases are considered, where the corner has a right-angle, and where the corner has been rounded with a 5mm radius-of-curvature. The current distributions computed by EFIT++ for each case is shown in figure 6. In the case of a right-angled corner, the current exhibits a singularity at the corner; whereas introducing finite curvature eliminates the rapid change in current. The variation of magnetic permeabilities shown in figure 7 exhibits a similarly rapid variation in the case of a right-angled corner, with the large corner current resulting in a local saturation with $\mu_r \approx 1$; rounding the corner removes the local saturation. Results of convergence tests for the case of a right-angle corner are shown in figure 8. Here fractional error is defined $\epsilon = 1/n_\epsilon \sum_{i=1}^{n_\epsilon} J(\ell_i) - J_{ref}(\ell_i)$ where $\{\ell_1, \ell_2, \ldots, n_\epsilon\}$ are a set of equally spaced points along the boundary, $J(\ell_i)$ is the boundary magnetisation current at $\ell_i$, $J_{ref}(\ell_i)$ is the reference value and $n_\epsilon = 10^5$. The figure demonstrates convergence with decreasing $h$ and constant $k$; also convergence with increasing $k$ provided that $h$ is sufficiently small. The use of higher-order elements has computational advantage for $\epsilon < 10^{-2}$

Figure 9 shows an example of multiple boundaries, in this case the locations of the JET iron boundaries to be analysed in sections 5 and 6. There are two closed boundaries and one open boundary, in each case the start of each boundary and the

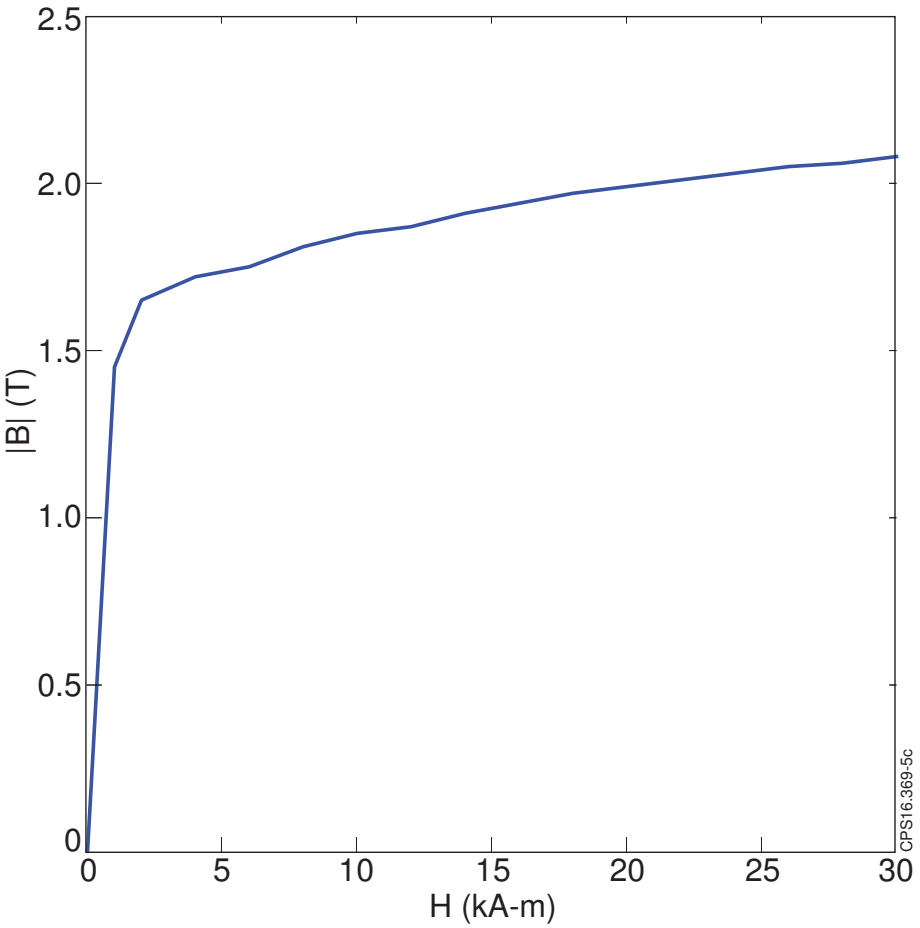


Figure 4: The B-H magnetic characteristic for the material boundary shown in figure 5.

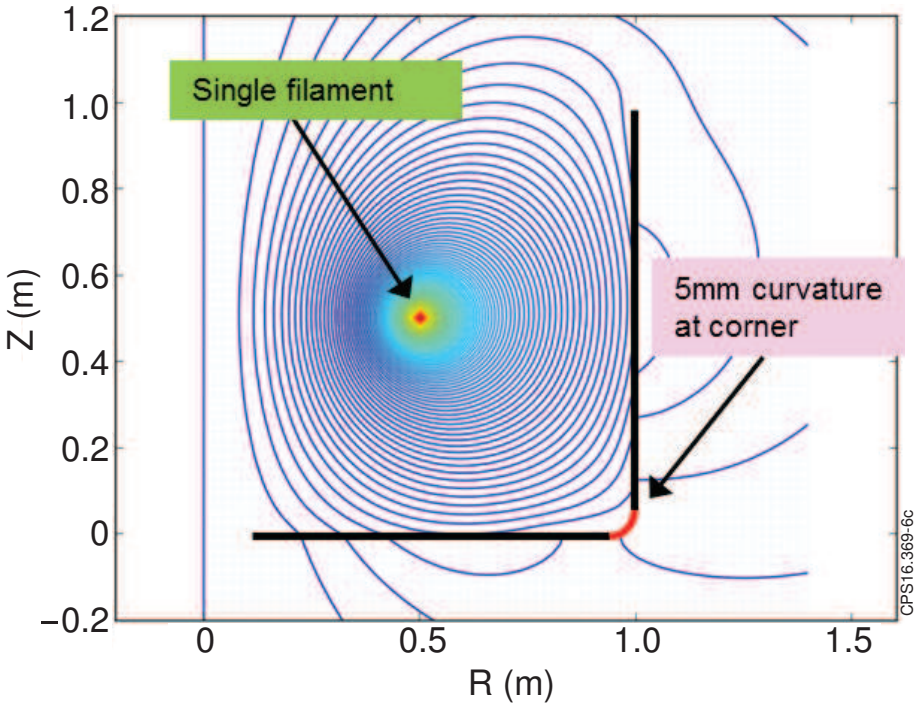


Figure 5: Contours of poloidal magnetic flux for the case of a single filament carrying 10MA close to a corner material boundary.

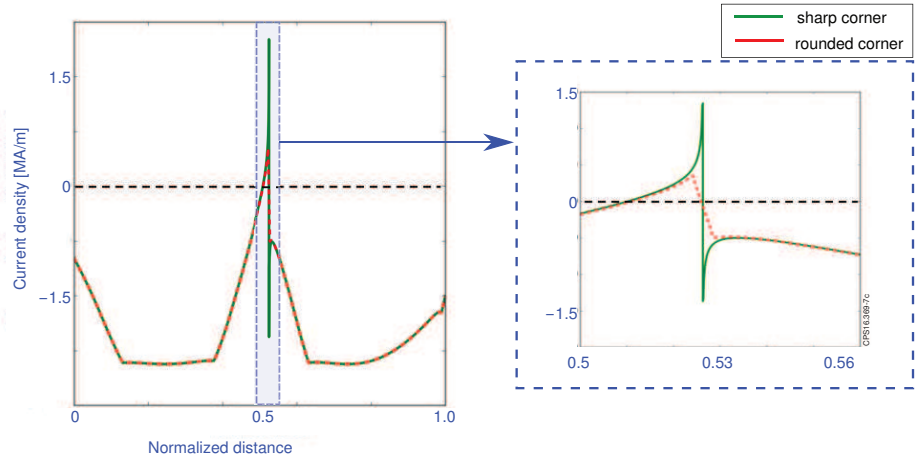


Figure 6: Current distribution on the material boundary for the case shown in figure 5. The boundary is traversed from $(R, Z)$=(1., 1.).

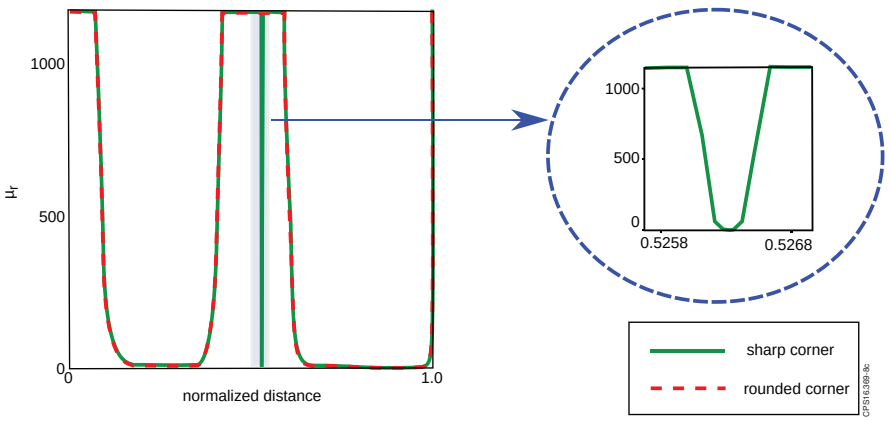


Figure 7: Variation of $\mu_r$ on the material boundary for the case shown in figure 5. The boundary is traversed from $(R, Z)$=(1., 1.).

direction of increasing $\ell$ is indicated. Whereas over most of each boundary there are straight-line segments, the pole pieces facing the plasma cavity are defined using arc segments with the radii of curvature indicated in red in the figure. The location of breakpoints is shown in figure 10; in this case the density of the breakpoints increases exponential towards corners. The basis functions shown in figures 2 and 3 are for the start of the inner boundary displayed in figure 9.

## 4. Internal magnetisation currents

In cylindrical coordinates the internal magnetisation current density (equation 16) can be written

$$J_\phi^\mu = \frac{\left(2B_rB_z\frac{\partial B_r}{\partial R} + (B_z^2 - B_r^2)\frac{\partial B_z}{\partial R} + \frac{B_r^2B_z}{R}\right)\frac{\partial \mu_r}{\partial |B|}}{\mu_r B_r^2 \frac{\partial \mu_r}{\partial |B|} - \mu_o\mu_r|B|} \tag{48}$$

in which $B_r$ and $B_z$ are components of the magnetic field vector $\mathbf{B} = B_r\hat{\mathbf{R}} + B_\phi\hat{\phi} + B_z\hat{\mathbf{Z}}$ and $|B| \equiv \sqrt{B_r^2 + B_z^2}$.

The following procedure is carried out to include the effect of $J_\phi^\mu$:

1. Using the mesh generator TRIANGLE[27] iron regions are covered with a triangular mesh of size $n_m$. As computational run times are dependent on the number of free parameters, it is advisable to employ a very coarse mesh and refine as necessary for the required accuracy in subsequent steps.
2. The triangular mesh forms the basis of a discretisation over the interior of the iron enabling $J_\phi^\mu$ to be approximated by a set of $n_m$ discrete current densities. Field values for each element are evaluated at its centroid.

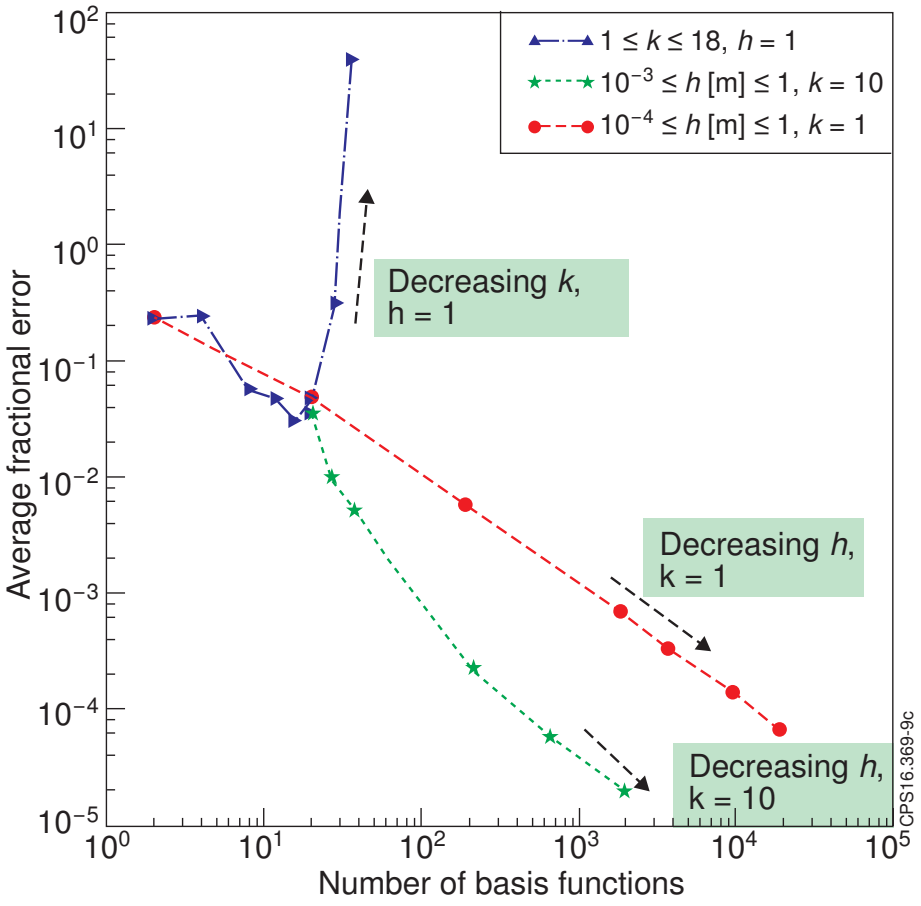


Figure 8: Dependence of fractional error ($\epsilon$) on $h$ and $k$ for the example shown in figure 5. (The parameters $h$ and $k$ are respectively the knot spacing and the order of the B-spline.) The figure demonstrates convergence with decreasing $h$ and constant $k$; also convergence with increasing $k$ provided that $h$ is sufficiently small. The use of higher-order elements has computational advantage for $\epsilon < 10^{-2}$

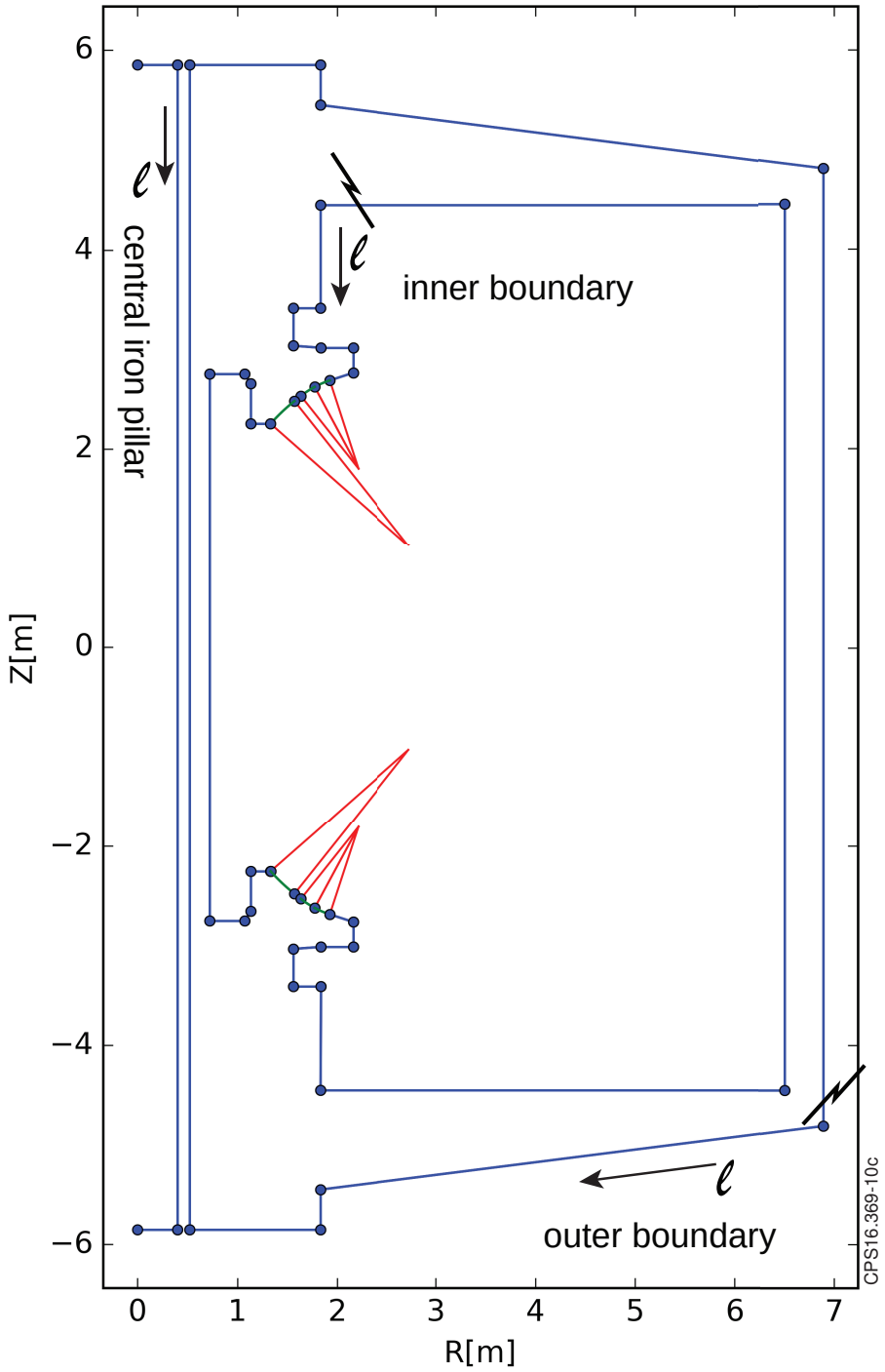


Figure 9: The locations of the JET iron boundaries analysed in sections 5 and 6. There are three boundaries: two closed boundaries and an open boundary.

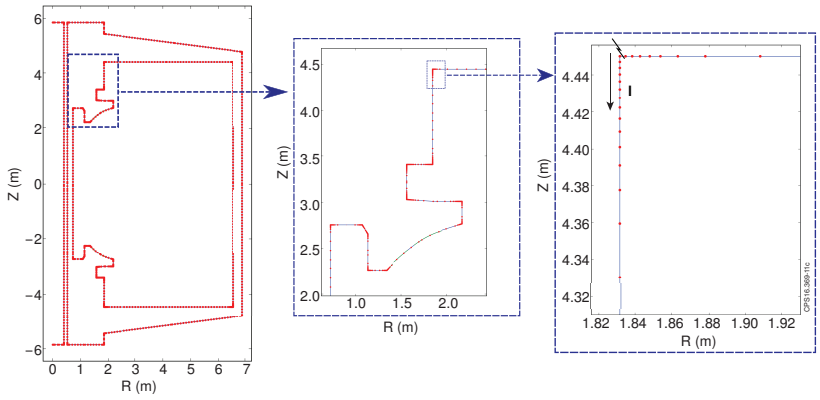


Figure 10: The locations of the breakpoints for the JET iron boundaries analysed in sections 5 and 6.

3. Figure 1a is a flow diagram for EFIT++. The internal magnetisation currents are computed in the step after solving for the boundary magnetisation currents. To improve computational speed tabulated response functions for each of the parameters appearing in equation 48 are computed and stored for subsequent runs.
4. Adaptive refinement of the triangular mesh is carried out by subdividing triangular elements that make the largest contribution to $\psi_p$ within the vacuum vessel (the primary region of interest). After each mesh refinement steps 2 to 4 are repeated until the system has converged, determined by the maximum change in the computed magnetic probe signals between mesh refinement steps.

Figure 11 shows an example of a triangular mesh for the cases analysed in sections 5 and 6. This mesh, with 231 elements was generated by TRIANGLE. Figure 12 shows a refined mesh generated by the above procedure with 4570 elements. Preliminary runs carried out of a simulated plasma discharge described in section 5 indicated that significant internal currents are present only close to the ends of the solenoid and at corners; consequently the mesh was placed in these regions and elsewhere $J^{\mu}_{\phi}$=0.

## 5. Validation of the deterministic magnetisation model

In order to validate the results of the EFIT++ deterministic magnetization model, a detailed code benchmark has been carried out between EFIT++ and the finite element code COMSOL Multiphysics [28]. The COMSOL Multiphysics AC/DC physics module is widely used to predict and design electric and magnetic fields in static and dynamic low-frequency applications in two-dimensional and three-dimensional spaces along with traditional circuit-based modelling of passive and active components. The main objective of this code benchmark is to validate the deterministic model by comparing it with a synthetic 2-D electromagnetic model of JET. The COMSOL Multiphysics 2D axisymmetric electromagnetic model of JET[29] is based on Maxwell's equations with appropriate boundary conditions at the physics interfaces of different

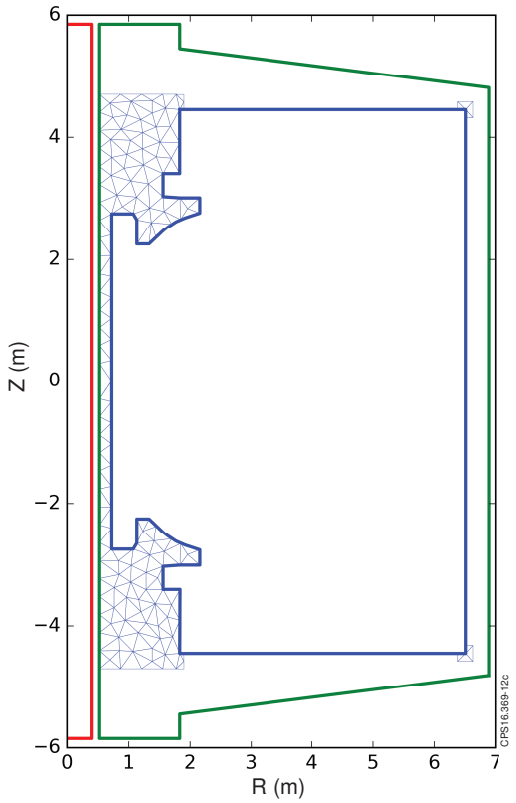


Figure 11: Initial triangular mesh generated by TRIANGLE with 231 elements used for the cases analysed in sections 5 and 6.

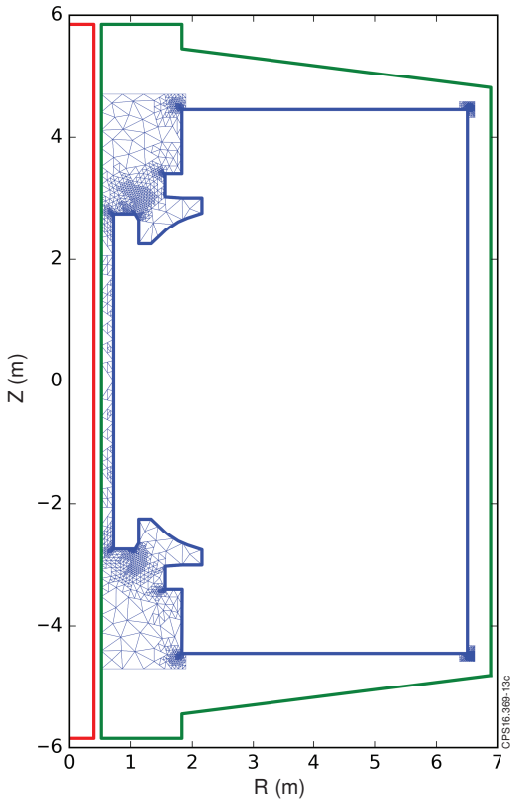


Figure 12: Triangular mesh with 4570 elements used to compute the internal magnetisation currents for the cases shown in sections 5 and 6.

material (air, iron-core, conductors) and components (poloidal field circuits, and passive conducting structures like vacuum vessel, the restraint rings, the mechanical structure, and the divertor supporting structure [30]).

Previous studies of the JET breakdown scenario using the CREATE code [30] provide a convenient comparison of the iron model implementation in COMSOL Multiphysics. Both the CREATE and COMSOL Multiphysics models of the JET iron take into account the presence of a gap in the upper magnetic circuit according to [29, 31]. The air-gap is not taken into account in the EFIT++ model, however comparisons between EFIT++ and COMSOL described later in this section show that the effect on the field is local. Figure 13 plots the magnetic characteristics of the ferromagnetic material. This is based on the available data of the dominant material used for the JET iron core, Nomatil RD[32]. Figure 14 shows a static COMSOL Multiphysics reconstruction of the magnetic topology for a JET breakdown configuration with prescribed primary (IP1) and vertical (IP4) circuit currents before the loop voltage application. The hexapolar flux structure and the magnetic null location are in good agreement with the results provided by the CREATE model as discussed in [29].

As COMSOL Multiphysics is not an equilibrium reconstruction code, for the purpose of the benchmark between EFIT++ and COMSOL Multiphysics the plasma current is represented as a lumped circuit element with constant current density enclosed in a 20cm by 20cm toroidal conductor at the geometric axis of the machine (R,Z)=(3.,0.). This setup is used because it can produce a magnetic topology similiar to an equilibrium reconstruction with results that can be directly compared between the two codes. Below we describe this approach to model JET discharge 82937. Figure 15 shows the time-traces of the poloidal field power supplies and plasma current. For details of the configuration see[33, 34] . Plasma breakdown occurs at 40s and the plasma current thereafter ramps up to a magnitude of 2MA.

Flux surfaces computed by EFIT++ at a number of times through the discharge are shown in figure 16 from just prior to breakdown (t=39.9s), during the plasma ramp-up (t= 42s), during the flat-top (t=52s) and in the latter part of the discharge (t=63s). The runs have 1442 piecewise constant ($k$=1) boundary elements and 4570 internal elements generated by iterative convergence using 25 time slices between t=39.9s and 63s. The choice of boundary and internal elements will be referred to below as the *high resolution* EFIT++ configuration.

Figure 17 shows the variation of the boundary magnetisation current and magnetic permeability at t=39.9 for the iron boundary facing the plasma traversing counter-clockwise from the top left-hand corner (R,Z)=(1.832,4.45). The local current density rises sharply near corners causing a local reduction in the value $\mu_r$ (ie. magnetic saturation). The increased current density at corners generates a non-local field contribution that must be resolved adequately. The implication is that the loading of knots must be increased close to corners.

Figure 18 show the variation of the internal magnetisation current corresponding to figure 16. There is a finite magnetization current close to internal corners lying near to the shortest path length for magnetic flux to circulate around the iron core. The sign of these current is in the same direction as the solenoid current indicating that the solenoid current is the primary cause of these internal magnetisation currents. In addition, above a threshold magnitude of solenoid current $|I_{p1}| \gtrsim$10kA, stripes of current appear at the

bottom and the top of the solenoid. These currents have opposite sign to the nearby corner currents and appear at the point at which the bulk of the iron changes from saturated to unsaturated state. Finally it should be noted that there are no significant currents in the pole pieces apart from close to the ends of the solenoid.

Figure 19 shows the magnitude of the discrepancy in magnetic flux between EFIT++ and COMSOL Multiphysics. The results show that agreement between EFIT++ and COMSOL Multiphysics in the *region of interest* (ie. close to and within the vacuum vessel) is always better than 0.1Wb; relative to the magnetic flux values (these are shown in figure 16 in units of Wb/rad) the discrepancy is less than 1% in the region of interest. In addition the results demonstrate that the effect of the air gaps introduces a local perturbation to the field that has only a marginal effect on the field in the region of interest.

Figure 20 shows the discrepancy in $\delta B = |\mathbf{B}_{\mathrm{EFIT++}} - \mathbf{B}_{\mathrm{COMSOL}}|$. The locations of the poloidal field coils are apparent as these are where the discrepancies are large; these discrepancies are a consequence of the finite element grid resolution used by COMSOL Multiphysics. This grid has been selected because it guarantees a converged solution in the region of interest for a minimum number of elements. Over the entire simulation, the maximum field discrepancy $\delta B$<1.5mT throughout the vacuum region. For comparison, this is the same magnitude as the toroidal field ripple which is 0.1% or 2-3mT[35]. The discrepancies of simulated magnetic probes signals is as follows: calculated signal accuracy is within 1% for signals with absolute magnitude >100mT; in all other cases agreement is to within 1mT. Figure 21 plots the same parameter, but this time the EFIT++ calculation ignores the internal magnetisation currents. The maximum discrepancy in the vacuum region has now increased to >20mT. This can result in an error of a computed magnetic probe around 5-10%, thus indicating the importance of including the internal magnetisation currents in the field calculation.

Figure 22 plots the measured and computed poloidal magnetic pickup coil signals at t=39.9s prior to plasma breakdown. These probes are situated adjacent to the vacuum vessel and parallel to its surface. The probes are approximately equally spaced, but without a detector on the outboard mid-plane; the first probe is at 60cm above the mid-plane and the probes are numbered in anticlockwise order. Details are given in table 1 and are indicated as red bullets in figure 1c. The calculated results purposely do not constrain to the measured magnetic data because the primary purpose is to validate the EFIT++ and COMSOL Multiphysics models against each other. The results confirm that the high resolution EFIT++ result and COMSOL Multiphysics result are in good agreement. Both calculations exhibit a significant discrepancy with the measured probe data; this is particularly apparent for probe 7 (situated towards the top inboard side of the vessel). The origin of these errors could be related to the axisymmetric nature of the 2D electromagnetic model, or the presence of locally induced currents, or other factors and is the subject of further investigations. The *low-resolution* EFIT++ calculation uses the determinsitic iron model with the intershot magnetisation configuration ie. a single iron boundary with 98 piece-wise constant elements and without internal magnetisation currents. The result indicates that the accuracy of this model is not suitable for analysing data in the absence of plasma current.

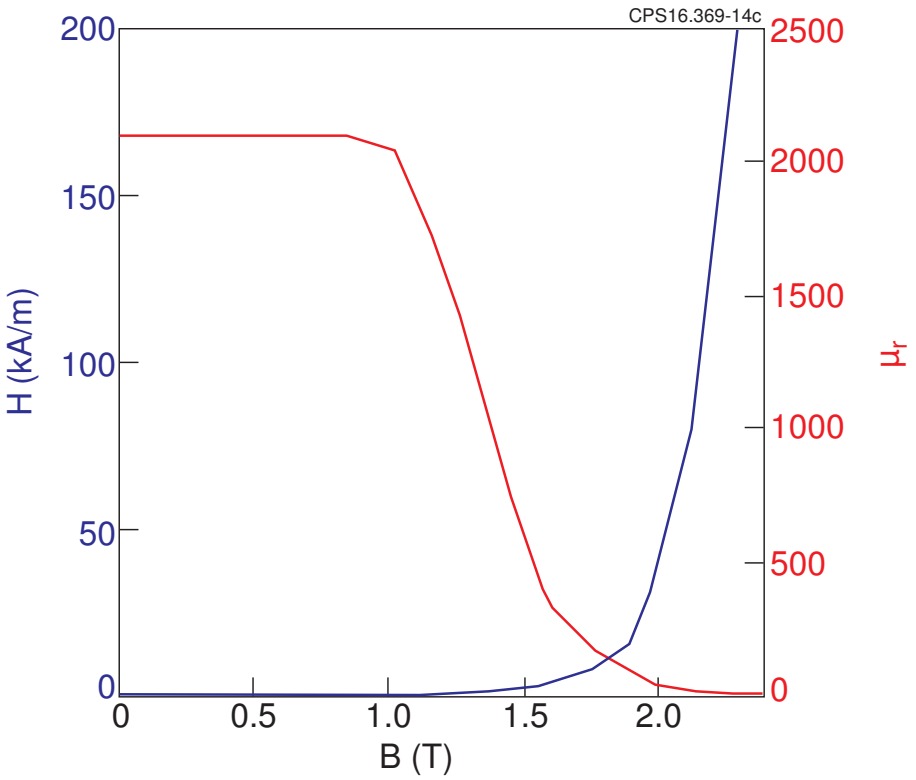


Figure 13: The magnetic characteristics of the iron in JET.

Table 1: Poloidal magnetic probes in JET. The orientation is the anticlockwise poloidal angle measured between the axis of the probe and $\hat{\mathbf{R}}$

| probe | R[m] | Z[m[ | orientation[deg] |
|---|---|---|---|
| BPME(1) | 4.292 | 0.604 | -74.1 |
| BPME(2) | 4.088 | 1.082 | -60.5 |
| BPME(3) | 3.779 | 1.498 | -47.0 |
| BPME(4) | 3.381 | 1.830 | -33.5 |
| BPME(5) | 2.815 | 2.092 | -13.2 |
| BPME(6) | 2.217 | 1.993 | 32.7 |
| BPME(7) | 1.864 | 1.493 | 75.4 |
| BPME(8) | 1.739 | 0.875 | 81.5 |
| BPME(9) | 1.679 | 0.247 | 87.6 |
| BPME(10) | 1.679 | -0.247 | 92.4 |
| BPME(11) | 1.739 | -0.875 | 98.5 |
| BPME(12) | 1.864 | -1.493 | 104.6 |
| BPME(13) | 2.217 | -1.993 | 147.3 |
| BPME(14) | 2.815 | -2.092 | -166.8 |
| BPME(15) | 3.381 | -1.830 | -146.5 |
| BPME(16) | 3.779 | -1.498 | -133.0 |
| BPME(17) | 4.088 | -1.082 | -119.5 |
| BPME(18) | 4.292 | -0.604 | -105.9 |

## 6. Equilibrium force-balance solution of JET discharge 91576

The deterministic magnetisation model has been used to study JET discharge 91576 in the lead up and and during its flat-top phase $53 < t[s] < 58$ when the plasma current $I_p$=1.5MA and deuterium neutral beam injected power, $P_{NBI}$=9MW. The plasma is in H-mode as is evident by regular ELM activity.

To assess the accuracy of the EFIT++ reconstructions, the results were compared to the separatrix outboard position and of the inner and outer strike-point positions. These values are themselves subject to some uncertainty as they are the result of numerical processing of measured data. The position of the outboard separatrix is obtained from the measured high resolution Thomson Scattering (HRTS) data as follows. Results from scrape-off-layer calculations [36] require that the electron temperature, $T_e$ at the separatrix is in the range $50 < T_e[eV] < 100$. The calculated location of the separatrix is obtained by fitting a quadratic function to the 8 outer non-zero HRTS channels. Uncertainties in the separatix position arises from three main sources, namely HRTS positional uncertainties, uncertainties in the separatrix electron temperature, and modeling errors. From repeat measurements of the system's absolute position calibration, uncertainties in the HRTS profile position are correct to ±1cm. Uncertainties arising from the choice of separatrix electron temperature can be deduced from plotting radial positions corresponding to 50eV and 100eV. Finally model uncertainties arising from the polynomial fit is estimated as the mean average error between the polynomial fit function and the data, and is indicated in the results presented. The strike-point

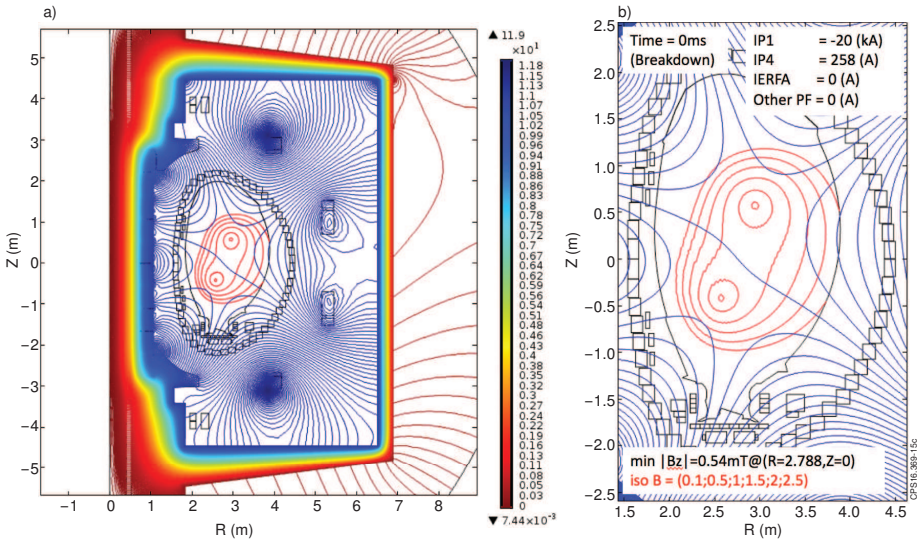


Figure 14: a) COMSOL Multiphysics reconstruction of the magnetic topology for a JET breakdown configuration with prescribed primary (IP1) and vertical (IP4) in units of V-s ; b) Detail of the hexapolar flux structure in the vacuum vessel (blue) and the magnetic field null location indicated by the iso-lines in mT (red)

positions are obtained by fitting the heat flux profile shape [37] to the infrared (IR) cameras KL9A and KL9B viewing the divertor. The spatial registration has an uncertainty within ±5mm of the measured position. An additional uncertainty arises from relating the peak heat intensity to the location of the magnetic strike point: heat diffuses across flux surfaces into the private flux region resulting in the peak heat flux intensity being displaced relative to the separatrix. Results of model calculations[37] predict that this displacement is ~2-3mm; results presented in this paper remove this offset when making comparisons with EFIT++ model calculations.

Equilibrium calculations were carried out using measurements from magnetic probes, flux loops and power supply currents using the deterministic model with the high resolution iron configuration described in section 5. EFIT++ was also run with the fitting model using the standard JET intershot run configuration; the magnetisation model in this case was configured with 98 piecewise constant boundary elements. The magnetic data set in the standard JET intershot has 35 magnetic probes, 4 flux loops, 27 saddle loops, and 10 measured power supply currents. The flux loops measure the total magnetic flux through a single toroidal loop at a given poloidal position, whereas the saddle loops measure the difference in magnetic flux between two toroidal loops. The flux loop, saddle loop and magnetic probe measurements are obtained by a hardware integration of the induced voltage signals. At the time that the integrators are initialised there are finite currents flowing in the poloidal field coils; these generate a contribution to the diagnostic signals that is not apparent in the measurement and is a source of error in the measured signals. Calculations using the EFIT++ deterministic iron model at this time predict that the errors resulting from this procedure are as follows: flux

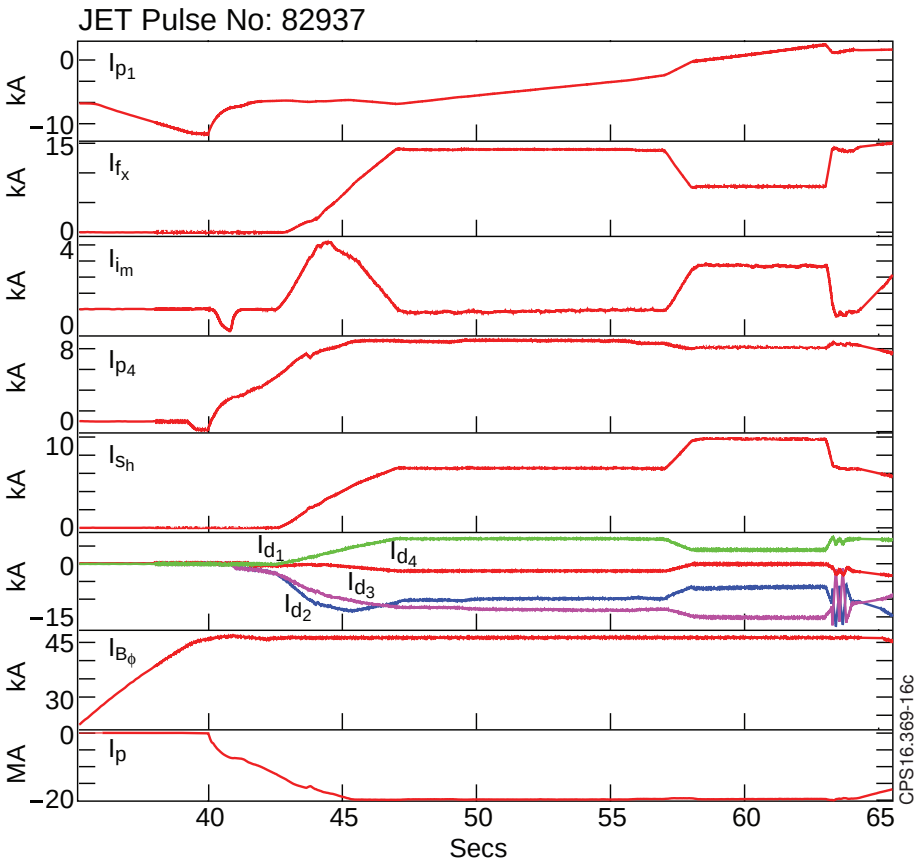


Figure 15: Time-traces of the power supply currents for JET discharge 82937. From top to bottom: $I_{p1}$ the solenoid current responsible for driving the majority of flux in the iron; $I_{fx}$ current also generates solenoidal field localised to the mid-plane; $I_{im}$ connected to coils at R=6m and configured to drive a radial field; $I_{p4}$ connected to coils at R=6m and configured to drive a vertical field; $I_{sh}$ generates a poloidal field specifically intendend to control the plasma shape; $I_{d1}$ to $I_{d_4}$ coils located in the divertor region control the strike point; $I_{B\phi}$ the toroidal field current; $I_p$ the plasma current.

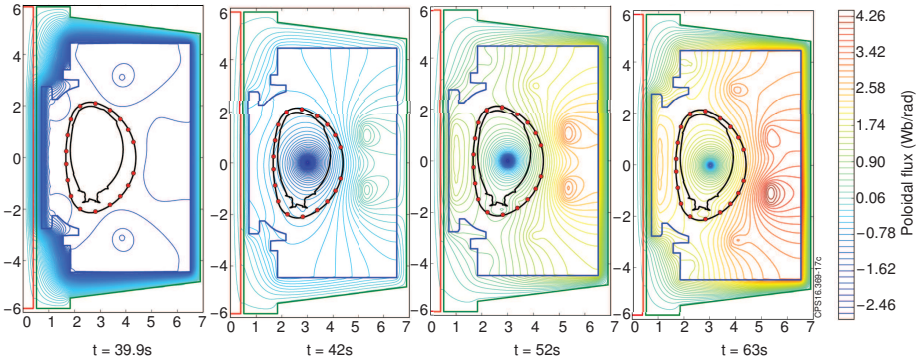


Figure 16: Contours of poloidal flux for JET discharge 82937. The plasma current (for $t$>39.9s) is assumed to flow in a rectangular toroidal conductor.

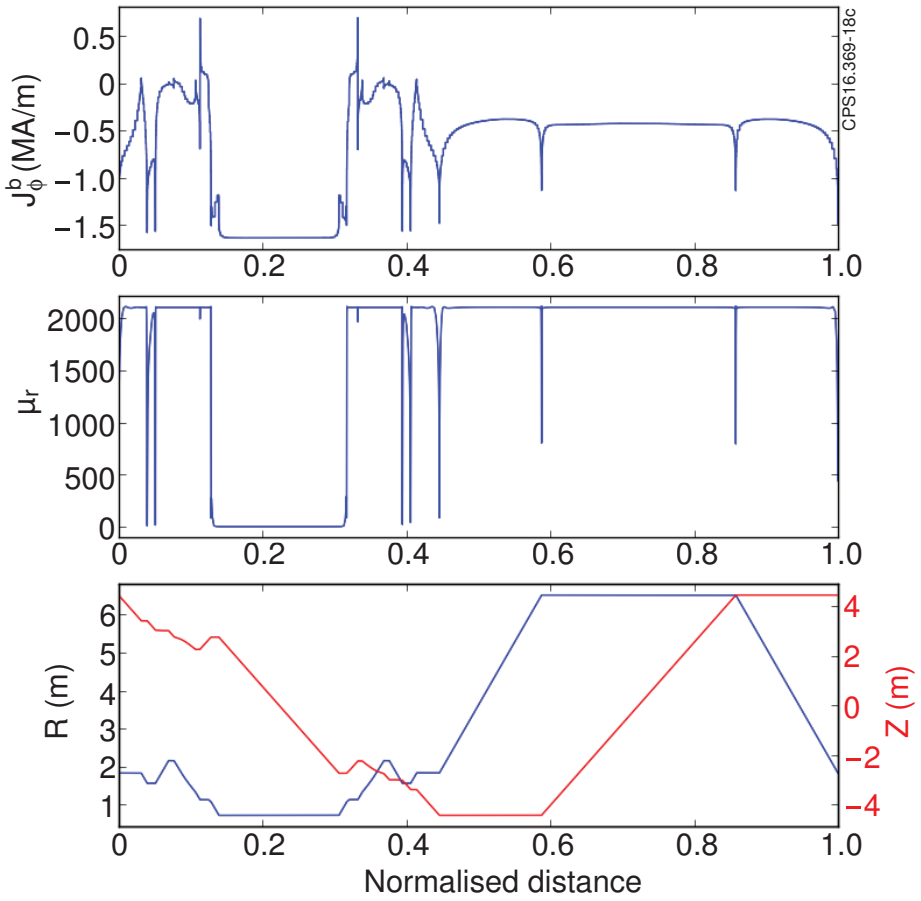


Figure 17: Variation of boundary magnetisation current and magnetic permeability for the iron boundary facing the plasma at t=39.9s in JET discharge 82937.

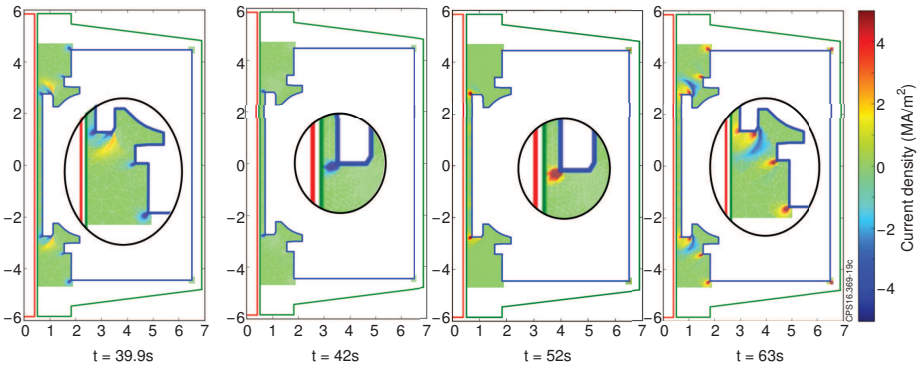


Figure 18: Internal magnetisation currents for JET discharge 82937 with the details at the lower pole shown in magnification. The plasma current (for $t$>39.9s) is assumed to flow in a rectangular toroidal conductor.

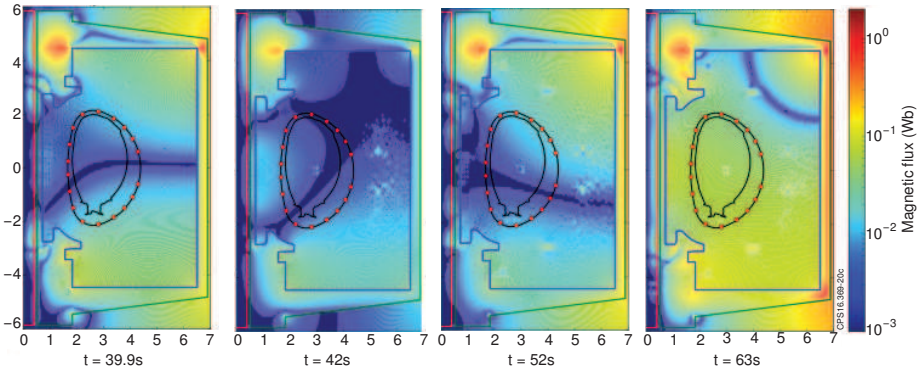


Figure 19: Magnitude of discrepancy in magnetic flux between EFIT++ and COMSOL for JET discharge 82937. The plasma current (for $t$>39.9s) is assumed to flow in a rectangular toroidal conductor.

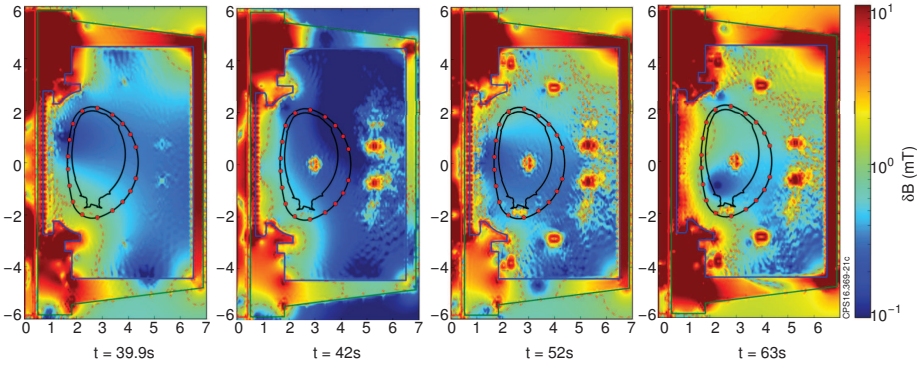


Figure 20: Discrepancy in $\delta B$ between EFIT++ and COMSOL Multiphysics for JET discharge 82937. The contour shown is for $\delta B$=1mT. The plasma current (for $t$>39.9s) is assumed to flow in a rectangular toroidal conductor.

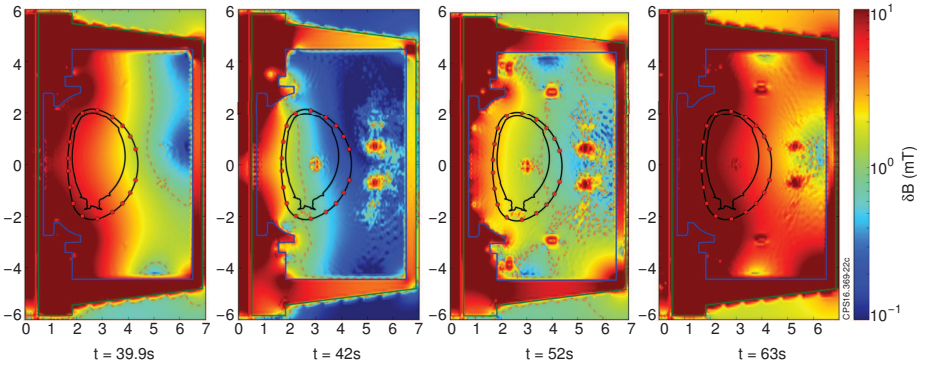


Figure 21: Discrepancy in $\delta B$ between EFIT++ and COMSOL Multiphysics for JET discharge 82937. Similar to figure 20 the plasma current is represented by a fixed dimension toroidal conductor. The EFIT++ run has not included the internal magnetisation currents. The plasma current (for $t$>39.9s) is assumed to flow in a rectangular toroidal conductor.

loops: 0.45Wb, saddle loops: <0.2mWB, magnetic probes: 1mT. With the exception of the flux loops, these discrepancies are small compared to the magnitude of the signal contribution from the plasma current; consequently the EFIT++ calculations presented in this section for the deterministic model exclude the flux loops. During initial runs of the deterministic model, two saddle loops measuring the difference in magnetic flux close to the mid-plane between the inner and outer vessel surfaces had individual $\chi^2$ values that were anomalously large, >35; in the fitting model the individual $\chi^2$ for these signals were <3. As there is some uncertainty in the calibration of the magnetic signals, the deterministic runs carried out excluded these two saddle loops. The results described below employ low order parameterisations for the plasma functions: $p' \propto 1 - \bar{\psi}_p$ and $ff' \propto 1 - \bar{\psi}_p$ as used in the intershot calculations on JET

Figure 23 shows a plot of the radial location of the outboard separatrix along the line-of-sight of the HRTS diagnostic. The standard intershot run exhibits a discrepancy of ~40mm. Excluding the 2 saddle loops and 4 flux loops, the discrepancy is reduced to 33mm. In comparison, the discrepancy for the deterministic model is 15mm which is compatible with the uncertainty of the HRTS alignment. Figure 24 shows a comparison of the outboard strike-point position. Results using the fitting model exhibit a constant discrepancy of ~30mm independent of whether the 4 flux loops and 2 saddle loops are included. The deterministic run has a much reduced discrepancy, between 0 and 10mm. The downward spikes seen in the plots are due to the intersection of the separatrix field line with the corner of a protruding tile at $R \approx 2.8$m. Finally figure 25 shows a comparison of the inboard strike point position. The IR-inferred inboard strike-point location fluctuates within a range of 30mm which is large compared to the fluctuations of inboard strike-point positions computed by the equilibrium reconstructions. Results of the fitting model using the standard inter-shot configuration lie within the range of the IR-inferred location and are insensitive to the inclusion of the flux loops and two saddle loops; in comparison results from the deterministic run lie just below the IR-inferred strike point.

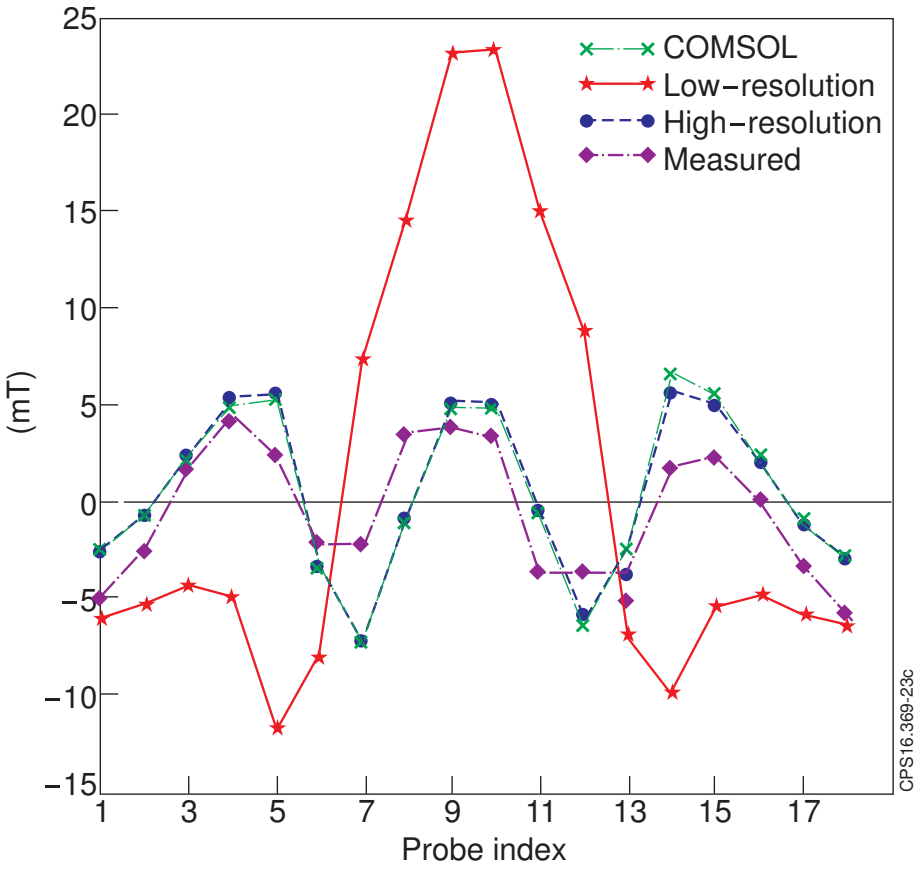


Figure 22: Computed and measured poloidal magnetic probe signals for JET discharge 82937 at $t$=39.9s just prior to plasma breakdown. The *high-resolution* and *low-resolution* traces are EFIT++ runs with deterministic iron model configured with respectively (a) 1442 boundary elements and 4570 internal elements and (b) 98 boundary elements on a single iron boundary and without internal magnetisation currents as used during intershot operation.

For the cases plotted in figures 23 to 25, the $\chi^2$ minimization calculations in EFIT++ have 12 and 110 free parameters respectively for the deterministic and fitting models arising from the 10 power supply currents, 2 plasma coefficients and (for the fitting model) the iron model. The larger number of free parameters in the fitting model enables it to absorb underlying errors in the measured signals. This is apparent in the plot of $<\chi^2>$ shown in figure 26. Here,

$$<\chi^2>=\frac{1}{n_m}\sum_{i=1}^{n_m}\left(\frac{M_i-C_i}{\sigma_i}\right)^2 \tag{49}$$

where $\sum$ denotes a summation over the $n_m$ measured data (but not the quasi-measurements in the case of the fitting model). The intershot run has $<\chi^2>$=0.25, suggesting that the error is a factor of two better than obtained from the underlying measurement calibrations; an alternative explaination is that the model is overfitting. The deterministic run has has a higher value $<\chi^2> \approx 1$. Whilst this is in the expected range, there is a linear variation in time that correlates with the variation of the P1 current. This may be due to a number of factors including calibration errors, parasitic pick up, or limitations of the 2-D treatment of the 3-D iron structure. Work is currently underway to understand this issue further.

Figure 27 plots the difference between the EFIT++ calculated signals and the measured signals for the poloidal probes discussed in section 5 and described in table 1. The figure shows clearly that the fit to the magnetic probes for the EFIT++ deterministic model is considerably poorer than for the fitting model, exhibiting discrepancies of up to 15mT or 5% of the measured signal magnitude. In addition, the graph shows evidence that the discrepancy has a systematic trend between the detectors. The explanation is currently being investigated: it could be due to an error in the applied external vertical field either from a calibration error in the P4 current or from a limitation of the 2-D electromagnetic model.

As stated earlier, the plasma parameterisations used in the equilibrium calculations describe the plasma in terms of just two degrees of freedom with the current density falling to zero at the separatrix. McCarthy et al. [38] have shown that magnetic measurements provide constraints on the edge-localised moments of the plasma current distribution and it is reasonable therefore to expect that the separatrix location will be influenced by the choice of plasma current parameterisation. To examine this issue further additional runs of the deterministic model were carried out with $p' = a_0 + a_1\bar{\psi}_p$ and $ff' = b_0 + b_1\bar{\psi}_p$ with $a_0$, $a_1$, $b_1$ and $b_2$ constants whose value is determined by the $\chi^2$ minimisation. This parameterisation permits finite pressure and current at the separatrix. The results of these runs were similar to before with the following differences: The calculation of the outboard separatrix position was within 1mm agreement; the outboard strikepoint position was shifted inward by 2mm, and the inboard strikepoint position was moved outward by 6mm. In all cases, these changes are small compared to the positional uncertainties inferred by HRTS, and the IR data. The lack of sensitivity of the results to the choice of the plasma function parameterisation is explained by the fact that even when a finite edge current is permitted by the choice of current parameterisation, the computed edge current is generally small. Whilst this result could suggest that the edge current is small for this discharge, results could also be affected by

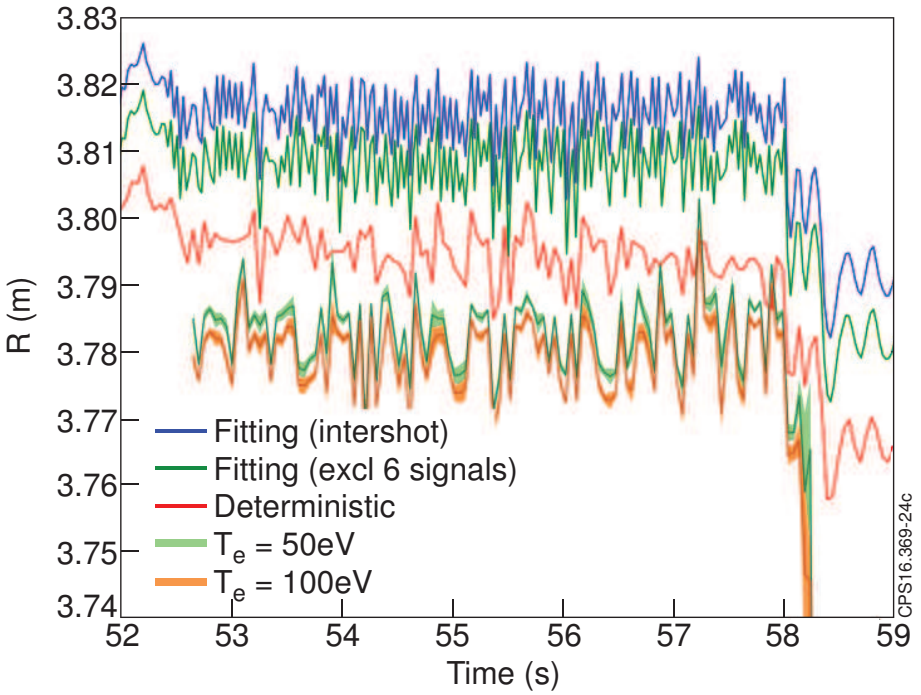


Figure 23: The radial location of the outboard separatrix along the line-of-sight of the HRTS diagnostic for JET discharge 91576. The radial location of $T_e$=50eV and $T_e$=100eV inferred from HRTS are the two lower traces. The EFIT++ results are as follows (a) *fitting (intershot)* uses the fitting model configured with the standard JET intershot settings; (b) *fitting (excl 6 signals)* uses the fitting model configured with the standard JET intershot settings but excluding 4 flux loops and 2 saddle loops; (c) *deterministic iron* uses the deterministic iron model with the same magnetic measurements as for case (b) .

systematic errors in the measurements; furthermore there is the possibility of strongly localised current spikes at the separatrix due to bootstrap currents[39], or of currents flowing outside of the separatrix. Whilst there is no direct evidence of either, theory[40] predicts bootstrap currents are larger in regions of steep density and temperature gradients. At the times of analysis, the plasma is in high-confinement (H-mode) regime with strong gradients close to the separatrix; this is apparent from the measurement of D-alpha emission showing the occurrence of ELMS at this time. Further studies are currently underway to examine these aspects and will be reported in a future paper.

## 7. Conclusions

In this paper an alternative solution for the free-boundary plasma equilibrium problem in the presence of ferromagnetic material based on measured constraints, named deterministic magnetisation model, has been introduced. The ferromagnetic material has been represented by a boundary current with the gradients in the magnetisation dipole state generating macroscopic internal magnetisation currents. A model for the

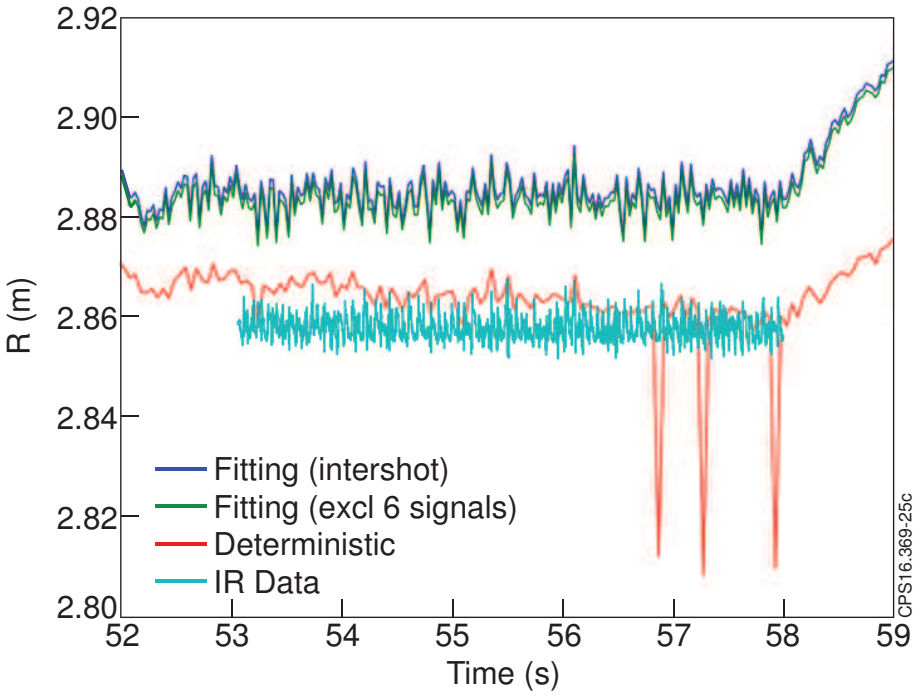


Figure 24: The radial location of the outboard strike-point for JET discharge 91576 The EFIT++ results are as follows (a) *fitting (intershot)* uses the fitting model configured with the standard JET intershot settings; (b) *fitting (excl 6 signals)* uses the fitting model configured with the standard JET intershot settings but excluding 4 flux loops and 2 saddle loops; (c) *deterministic iron* uses the deterministic iron model with the same magnetic measurements as for case (b) .

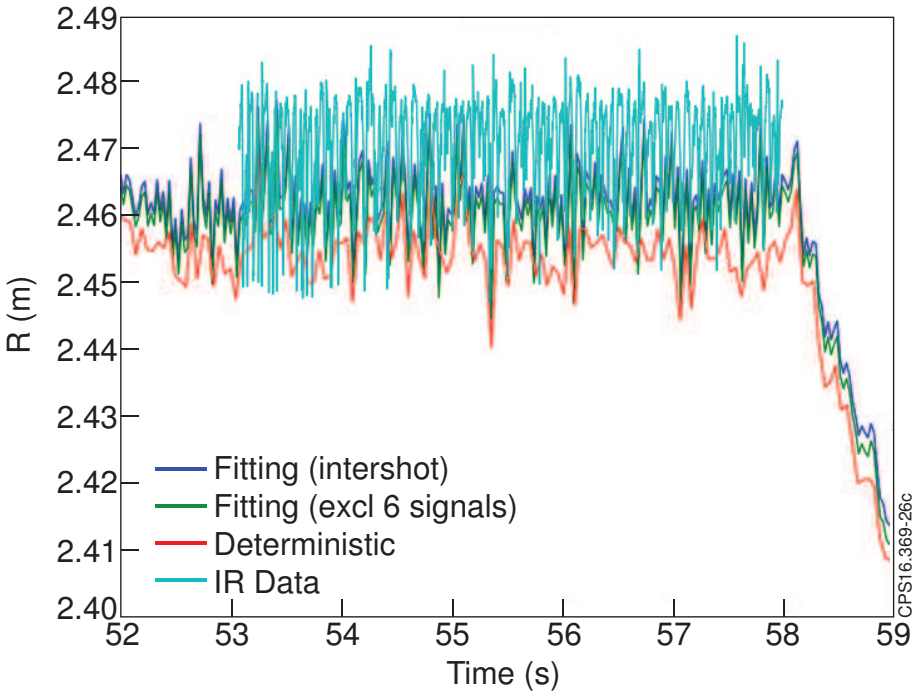


Figure 25: The radial location of the inboard strike-point for JET discharge 91576. The EFIT++ results are as follows The EFIT++ results are as follows (a) *fitting (intershot)* uses the fitting model configured with the standard JET intershot settings; (b) *fitting (excl 6 signals)* uses the fitting model configured with the standard JET intershot settings but excluding 4 flux loops and 2 saddle loops; (c) *deterministic iron* uses the deterministic iron model with the same magnetic measurements as for case (b) .

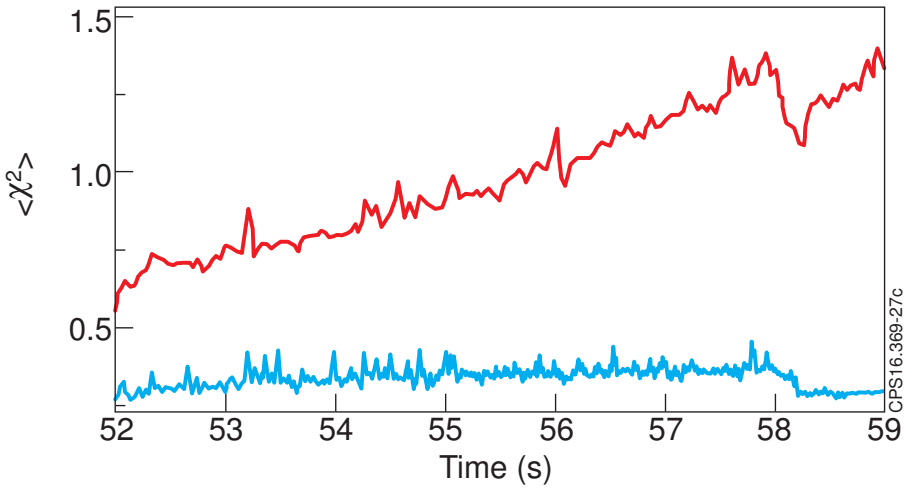


Figure 26: Time-variation of $< \chi^2 >$ for JET discharge 91576. The EFIT++ results are as follows (a) in cyan, uses the fitting model configured with the standard intershot settings (b) in red, uses the deterministic iron model.


| | BPME(1) | BPME(2) | BPME(3) | BPME(4) | BPME(5) | BPME(6) | BPME(7) | BPME(8) | BPME(9) | BPME(10) | BPME(11) | BPME(12) | BPME(13) | BPME(14) | BPME(15) | BPME(16) | BPME(17) | BPME(18) |
|---|---|---|---|---|---|---|---|---|---|---|---|---|---|---|---|---|---|---|
| deterministic | -5.9 | -8.4 | -6.6 | -3.2 | -3.4 | -0.3 | 3.6 | 14.3 | 5.7 | 3.9 | 8 | 6.9 | 4.1 | -6.1 | 2.5 | -7.1 | -8.8 | -9 |
| fitting (intershot) | -0.6 | -2 | -0.9 | 0.7 | -0.6 | -0.2 | -1 | 1.9 | -2.6 | -2.8 | -0.2 | 1.2 | 1.6 | -1.5 | 6 | -2.7 | -3.2 | -4.1 |
| fitting (excl 6 signals) | -1 | -2.4 | -1.1 | 0.8 | -1 | -0.3 | -0.6 | 1.7 | -2.5 | -2.5 | -0.4 | 1 | 1.3 | -1.6 | 5.1 | -3.2 | -3.4 | -4.1 |

CP516.369-60c

Figure 27: Poloidal probes signals for JET discharge 91576 at t=55.028s during the flat-top. The plot shows EFIT++ calculated signals with measurements subtracted. (i) deterministic model configured with the standard JET intershot settings but excluding 4 flux loops and 2 saddle loops; (ii) fitting iron model with the same magnetic measurements as for case (i); (iii) fitting model configured with the standard JET intershot settings;

boundary magnetisation currents at the iron-air interface has been developed using B-Splines enabling continuity to arbitrary order; internal magnetisation currents have been allocated to triangulated regions within the iron, and a method to enable adaptive refinement has been implemented. The deterministic model has been validated by comparing it with a synthetic 2-D electromagnetic model of JET. It is shown that the maximum field discrepancy is less than 1.5mT throughout the vacuum region enclosing the plasma. The discrepancies of simulated magnetic probe signals are accurate to within 1% for signals with absolute magnitude greater than 100mT; in all other cases agreement is to within 1mT. Moreover, the failure to take into account the presence of internal magnetisation currents due to the gradients in the magnetisation dipole state can lead to significant model errors >20mT around 5-10% of measured probe signals. The discrepancy of the poloidal magnetic flux within the vacuum vessel is to within 0.1Wb. The deterministic magnetisation model has been applied to an equilibrium force-balance solution of a JET discharge. The results are a significant improvement over the intershot EFIT++ runs for fitting to HRTS and IR inferred strike-point locations and outboard mid-plane position of the separatrix. This is an important result since prior work has only achieved good fits by simultaneously fitting to *kinetic* constraints such as polarimetry, MSE or pressure profiles [41].

The fact that generally the deterministic model has far fewer degrees of freedom (in the case studied in section 6 the reduction is in the ratio 12:110) makes it all the more remarkable that the deterministic model provides improved agreement with HRTS and IR data. The reduction in the degrees of freedom leads to an increase in $< \chi^2 >$, increased systematic errors and indications of the presence of drift in the magnetic signals. As a corollary, the large number of free parameters in the fitting magnetisation model have the possibility of absorbing inconsistencies in the data making systematic errors difficult to identify. Analysis of the uncertainties associated with the HRTS and IR data supports the view that these non-magnetic measurements provide more reliable

positions for the outboard separatrix and strike points than the magnetic signals. Future work will be to identify the origin of the inconsistencies using plasma *dry-runs* to improve the calibration of the data signals.

## 8. Acknowledgements

The authors wish to thank Lang Lao for his initial development of the EFIT code; Sergei Gerasimov for useful discussions regarding magnetic diagnostics on JET; Scott Silburn for the use of Infrared Camera data; Joanne Flanagan for the use of HRTS data; Emilia Solano for discussions on magnetic equilibria over many years and for alerting the authors to the particular challenges of obtaining equilibrium reconstructions on JET; also grateful thanks to Francesco Maviglia and Giovanni Artaserse for discussions on the iron core at JET and comparisons carried out with the CREATE code. Finally the authors wish to acknowledge Gabor Szepesi for his work as Responsible Officer for JET equilibrium reconstruction and hence his concomitant experience of the practical difficulties. This work has been carried out within the framework of the EUROfusion Consortium and has received funding from the Euratom research and training programme 2014-2018 under grant agreement No 633053 and from the RCUK Energy Programme [grant number EP/P012450/1]. To obtain further information on the data and models underlying this paper please contact PublicationsManager@ccfe.ac.uk. The views and opinions expressed herein do not necessarily reflect those of the European Commission.

## References

[1] D. O'Brien, L. Lao, E. Solano, M. Garribba, T. Taylor, J. Cordey, J. Ellis, Nuclear Fusion 32 (8) (1992) 1351.

[2] H. Fernandes, C. Varandas, J. Cabral, Brazilian Journal of Physics 32 (1) (2002) 100–106.

[3] P. Hertout, T. Pelletier, F. Saint-Laurent, F. Rimini, J. Bucalossi, Fusion Engineering and Design 74 (1-4) (2005) 671–677.

[4] O. Mitaraia, Y. Dingb, M. Hubenyb, T. O. Y. Lu and, D. McCollb, C. Xiaob, A. Hiroseb, Fusion Engineering and Design 89 (9-10) (2014) 2467–2471.

[5] E. Solano, G. Neilson, L. Lao, Nuclear Fusion 30 (6) (1990) 1107.

[6] L. L. Lao, H. S. John, R. D. Stambaugh, A. G. Kellman, W. Pfeiffer, Nuclear Fusion 25 (1985) 1611.

[7] L. C. Appel, M. K. Bevir, M. J. Walsh, Nuclear Fusion 41 (2001) 169.

[8] W. Zwingmann, Nuclear Fusion 43 (9) (2003) 842–850.

[9] L. C. Appel, G. T. A. Huysmans, L. L. Lao, P. J. McCarthy, D. G. Muir, E. R. Solano, J. Storrs, D. Taylor, W. Zwingmann, C. to the EFDA W. Zwingmann, R. Coelho, V. Drozdov, L.-G. Eriksson, B. Guillerminet, P. Huynh, G. Huysmans, C. Konz, F. Imbeaux, D. McDonald, P. Navaro, W. Schippers, J. Signoret, P. Strand, J. E. contributors, Equilibrium reconstruction code EQUAL with a scientific workflow system, in: 37th EPS conference on plasma physics, Dublin, Vol. 34, 2010, pp. P–4.180.

[10] P. J. McCarthy, P. Martin, W. Schneider, The cliste interpretive equilibrium code, IPP report nr. 5/85, Max-Planck-Institut fur Plasmaphysik (1999).

[11] K. Bosak, Real-time numerical identication of plasma in tokamak fusion reactor, Master thesis, University of Wroclaw, Poland (2001).
URL http://panoramix.ift.uni.wroc.pl/~bosy/mgr/mgr.pdf

[12] K. Bosak, J. Blum, E. Joffrin, F. Sartori, Real-time plasma magnetic equilibrium reconstruction for tokamaks, in: 27th EPS Conference on plasma physics, Saint-Petersbourg, Vol. 27a, 2003, pp. P–3.164.

[13] J. Blum, K. Bosak, E. Joffrin, New applications of equinox code for real-time plasma equilibrium and profile reconstruction for tokamaks, in: 12th ICPP International Congress on plasma physics, Nice, 2004.

[14] L. C. Appel, G. T. A. Huysmans, L. L. Lao, P. J. McCarthy, D. G. Muir, E. R. Solano, J. Storrs, D. Taylor, W. Zwingmann, C. to the EFDA Integrated Tokamak Modelling Task Force, J. contributors., A unified approach to equilibrium reconstruction, in: 33rd EPS conference on plasma physics, Rome, Vol. 30I, 2006, pp. P–2.184.

[15] W. R. Smythe, Static and dynamic Electricity, McGraw-Hill, New York, 1950.

[16] A. . K. Cline, Commun. Assoc. Computing Machinery 17 (1974) 218.

[17] O. Buneman, A compact non-iterative poisson-solver, Suipr report 294, Stanford University (1969).

[18] L. Lao, J. Ferron, R. Groebner, W. Howl, H. S. John, E. Strait, T. Taylor, Nuclear Fusion 30 (6) (1990) 1035.

[19] E. Anderson, Z. Bai, C. Bischof, S. Blackford, J. Demmel, J. Dongarra, J. Du Croz, A. Greenbaum, S. Hammarling, A. McKenney, D. Sorensen, LAPACK Users' Guide, 3rd Edition, Society for Industrial and Applied Mathematics, Philadelphia, PA, 1999.

[20] D. J. Griffiths, Introduction to Electrodynamics, 3rd Edition, Prentice Halll, New Jersey, 1999.

[21] G. Fix, S. Gulati, G. Wakoff, Journal of Computational Physics 13 (2) (1973) 209–228. doi:10.1016/0021-9991(73)90023-5, [link].
URL http://www.sciencedirect.com/science/article/pii/0021999173900235

[22] C. D. Boor, Journal of Approximation Thoery 50-62 (1972) 50.

[23] M. Cox, Journal of the Institute of Mathematics and Its Applications (current archive is maintained by IMA journal of Applied mathematics) 21 (1978) 135.

[24] H. Bachau, E. Cormier, P. Decleva, J. E. Hansen, F. Martín, Applications of B -splines in atomic and molecular physics, Reports on Progress in Physics 64 (12) (2001) 1815–1943. doi:10.1088/0034-4885/64/12/205.
URL http://stacks.iop.org/0034-4885/64/i=12/a=205?key=crossref.2257eec0e5040fc21410a9ef6e58af89

[25] C. de Boor, A practical guide to splines, revised Edition, Springer-Verlag, New York, 2001.

[26] W. Press, B. P. Flannery, S. A. Teukolsk, Numerical Recipes in FORTRAN: The Art of Scientific Computing, 2nd Edition, Cambrudge University Press, Boston, PA, 1992.

[27] J. R. Shewchuk, Computational Geometry: Theory and Applications 22 (1-3) (2002) 21–74.

[28] The COMSOL multiphysics modelling software, https://www.comsol.com.

[29] F. Maviglia, Electromagnetic models of plasma breakdown in the JET tokamak, IEEE Transactions on Magnetics 50 (2) (2014) 7023204.

[30] R. Albanese, F. Villone, Nuclear Fusion 38 (5) (1998) 723. [link].
URL http://stacks.iop.org/0029-5515/38/i=5/a=307

[31] F. Maviglia, R. Albanese, A. Alonso, P. Lomas, Fusion Engineering and Design 86 (6-8) (2011) 675–679.

[32] A. Quercia, R. Fresa, Fusion Science and Technology 61 (4) (2012) 257–274.

[33] E. B. et al., Fusion Technology 11 (1987) 94.

[34] E. B. et al., The JET divertor coils, JET-P(91) 26, JET (1991).

[35] G. Sadler, P. Barabaschi, E. Bertolini, S. Conroy, S. Corti, E. Deksnis, K. J. Dietz, H. P. L. de Esch, A. Gondhalekar, B. Green, M. Huart, M. Huguet, J. Jacquinot, O. N. Jarvis, A. Khudoleev, M. J. Loughlin, R. Konig, J. Last, A. Maas, M. Petrov, S. Putvinskii, C. Sborchia, D. Stork, B. Tubbing, P. van Belle, Plasma Physics and Controlled Fusion 34 (13) (1992) 1971.

[36] A. Kallenbach, N. Asakura, A. Kirk, A. Korotkov, M. Mahdavi, D. Mossessian, G. Porter, Journal of Nuclear Materials 337-339 (2005) 281.

[37] T. Eich, B. Sieglin, A. Scarabosio, W. Fundamenski, R. J. Goldston, A. Herrmann, Phys. Rev. Lett. 107 (2011) 215001. doi:10.1103/PhysRevLett.107.215001, [link].
URL http://link.aps.org/doi/10.1103/PhysRevLett.107.215001

[38] P. McCarthy, A. U. Team, Plasma Physics and Controlled Fusion 54 (2012) 015010.

[39] K. Miyamotor, Plasma Physics and Controlled Nuclear Fusion, Springer-Verlag, New York, 2005.

[40] O. Sauter, C. Angioni, Physics of Plasmas 6 (7) (1999) 2834.

[41] M. Brix, N. C. Hawkes, A. Boboc, V. Drozdov, S. E. Sharapov, J.-E. Contributors, Rev. Scientific Instruments 79 (2081) 10F325. doi:http://doi.org/10.1063/1.2964180.